Structural Health Monitoring of the Marine Structure Using Guided Wave and UAV-based testing

by

Yugansh Gupta

B. Tech., Yashwantrao Chavan Maharashtra Open University ,2014

Thesis Submitted in Partial Fulfillment

of the Requirements for the Degree of

MASTER OF ENGINEERING

in the Department of Mechanical Engineering

Supervisory Committee

Structural Health Monitoring of Marine Structures Using Guided Wave and UAV-based testing

by

Yugansh Gupta

B. Tech., Yashwantrao Chavan Maharashtra Open University (YCMOU) (MIT, MANET), 2014

Supervisory Committee

Dr. Yang shi, Department of Mechanical Engineering

Supervisor

Dr. Rishi Gupta, Department of Civil Engineering

Co-Supervisor

Abstract

The marine industry encompasses a vast range of structures that can be challenging to access, and thus highly mobile systems can be useful for efficient structural health monitoring. This research aims to investigate the feasibility of using unmanned aerial vehicles (UAVs) for deploying various non-destructive testing (NDT) methods to inspect steel structures. In addition, we are evaluating piezoelectric patches (PZT) based detection systems that can provide early warnings of corrosion and fatigue cracks. The study analyzes the pitch and catches method using time-of-flight (TOF) to detect cracks and defects, the UAV-based hammer percussion test for frequency response, and the use of an infrared-mounted camera on the drone for NDT purposes. The goal is to identify the best approach for monitoring the health of marine structures.

Supervisory Committee

Candidate: Yugansh Gupta

Supervisor: Dr. Yang Shi (Department of mechanical Engineering)

Co-supervisor: Dr. Rishi Gupta (Department of Civil Engineering)

Table of Contents

List of Tables

List of Figures

Acknowledgements

I am writing to express my sincere gratitude to Dr Yang Shi for giving me an opportunity to study at the University of Victoria and for your kind support and motivating words. I'm truly thankful to Dr Rishi Gupta for accepting me in his research lab, for constructive feedback, and for thoughtful advice through out my research work at the university. I also appreciate the time and effort Dr Gupta has invested in me, whether it was through answering my questions, reviewing my work, or providing additional resources to enhance my understanding.

I would like to thank Prakriti, a doctoral researcher at the University of Victoria, for her generous assistance and providing materials for the Master's project. At last, I would like to express my gratitude to all professors, co-workers, and friends who provided guidance and support during my studies.

Dedication

I dedicated this research work to God and my parents; without them in my life, I would not be able to do anything. I cannot express my immense gratitude to my brothers, Jayant and Saurabh Gupta, who have been strong pillars in all paths of my life. I would also like to thank my partner, Claudia, for her support and love.

1 Introduction

1.1 Background and motivation-

The foundation of international trade and the world economy is maritime transit [1]. Around 80% of world trade by volume and more than 70% by value are transported by sea and handled by ports worldwide [2]. All cargo vessels are mainly affected by two types of defects: Fatigue cracks and corrosion. Fatigue cracks can develop at welds, bolt holes, and cross-sectional changes as well as in the area of maximum stress from overloading. In addition, corrosion-induced cracking is frequently observed close to the surface of steel where the material has been weakened by corrosion [75]. If we fail to detect the these cracks and don't repair in time, it can lead to sudden catastrophic failure. The integrity of the marine structure can be significantly reduced due to the corrosive environment. Corrosion can also be caused by external factors such as seawater, tides, and the sea atmosphere, as well as from inside due to the carrying of ballast, fuel oil, and corrosive cargo [3].

To prevent significant damage and accidents, inspection by the class-approved third party should be carried out periodically, depending upon the vessel's age [5]. These inspections include an Annual survey (every year), an Intermediate survey (After 2-3 years), and a special survey (Every five years), which can last from days to weeks [4]. This inspection has a high monetary cost and risks human life, as it becomes more challenging to guarantee safety for the inspector [3]. To conduct a thorough visual inspection, the surveyor must be in close proximity to the part being examined, typically within arm's length. The surveyor relies on their experience to visually assess any structural damage, pitting, or corrosion. The inspection is recorded using various tools such as cameras for capturing images, chalk and pen for marking defects, and a clipboard for taking notes [6].

At the time of periodic inspection, the vessel needs to discharge the cargo; the tank must be gas-free and suitable for man entry. The vessel must be empty and positioned at a dockyard where scaffolding is

set up to provide human inspectors access to the areas of the vessel construction, which may be higher than 30 m, in order to complete this work. Also, to provide access to the surveyor for a comprehensive examination of the ship hull, extensive scaffolding must be built in the cargo hold [75]. Prior to the ship's inspection, the surveyor may have to wait a few weeks for the scaffolding to be put in place. Understandably, the charges for such time-consuming inspections are significant since the ship owner would waste money every day the ship is moored.

Third-party vendors, approved by the classification society, inspect inside the tank and also carry out a visual inspection of a certain area. Ultrasonic thickness monitoring (UTM) of the specific region in the ship structure is carried out by the inspector, as the visual inspection of the whole ship plate is time-consuming and difficult to access. Also, visual inspection has its limitations as it can only tell the surface condition but doesn't highlight subsurface defects. To illustrate the enormity of the visual inspection task, surveying a central cargo tank on huge cargo carriers can mean the visual assessment of more than 600,000 sq. m of steel [5]. So visual inspection is not an ideal method; that's why the shipping industry currently uses UTM.

UTM has certain limitations as it can only tell the thickness of the ship hull after metal reduction due to corrosion and erosion. The UTM is carried out on a certain designated point to detect a reduction in the metal plate and the rest of the ship's seaworthiness, decided by the visual inspection of the access area and age of the ship. Apart from that, the complicated structure makes it challenging to access every corner of the ship [120]. The surveyor's safety is at risk due to Carbon monoxide, H2S and benzene, some fatal gases inside the tank due to the type of cargo and fuel the vessel carries. Encountering those gases can cause fatality for the surveyor surveying the structural condition.

The entire cost of the infrastructure required for up-close examination of the hull on some types of vessels might be as high as $100,000 (e.g., ultra-large crude carriers) [6]. It follows that any level of

automation of the inspection process that can result in a reduction of inspection time, a decrease in financial costs, and/or an enhancement in the operation's safety is wholly warranted.

1.2 Objectives

The primary goal of this research is to find the best solution for structural health monitoring(SHM) of the ship's structure without requiring personnel to enter restricted areas. Various methods for continuous health monitoring and NDT methods are explored in this research work to find the ideal solution for the health monitoring of the marine structure.

1.3 Thesis outline

The thesis is organized as follows. The purpose, scope, and objectives of this study are briefly described in Chapter 1. In Chapter 2, the marine structure and the need for structural health monitoring are explored, followed by a review of the existing NDT techniques for steel structures. An introduction to the guided wave propagation method by using piezoelectric patches is explored to understand how piezoelectric patches can be effective in structural health monitoring in marine environments. Then, robotics-based non-destructive testing is explored, which discusses the introduction and advancement of defect detection on marine vessels. The chapter 3 explains the experimental investigation and highlights the work done on the acquired datasets to fulfil the objectives. Chapter 4 summarises the results and gives the optimum solution for structural health monitoring. Chapter 5 provides the conclusions drawn from this study and the possible future work to extend this study.

2 Literature review:

2.1 Structural health monitoring of the marine structure

Over time, the reliability of mechanical structures can decrease due to both working conditions and the surrounding environment. Degradation processes such as corrosion, fatigue cracks, erosion, and strength reduction can affect the integrity of these structures [9]. The magnitude and severity of these degradations depend on various factors, such as operating parameters, applied stresses, and material properties (e.g., corrosion resistance, microstructure, crystallographic orientation, and grain boundary structure) [10]. In the past, mechanical structural inspection and maintenance mostly relied on a preventive (time-based) approach. However, structural health monitoring (SHM) methodologies have gained importance in recent years to assess the health, predict the remaining usable life (RUL), and perform condition-based maintenance (CBM) of deteriorating structure [11].

The most common problems encountered by ships and offshore structures are corrosion and fatigue cracks. Without adequate monitoring and repair, these modes of degradation can cause catastrophic failure and shorten the structures' lifespan before their expected operational time [8]. Corrosion can weaken a ship's hull and offshore structure by reducing the section modulus of primary structural members. This reduction impairs the system's ability to resist external bending moments. Fatigue cracks, on the other hand, can impair the effectiveness of a structural element once the damage reaches a critical size.

The estimation of a ship's or offshore structure's lifespan is significantly influenced by the loss of section thickness for structural elements and the potential for integrity loss due to pitting corrosion. Pitting corrosion is the most dangerous type of corrosion in marine structures. Please refer to the table below for further information on the various types of corrosion in marine structures [7].

Table 1: various types of corrosion and defect in marine structure

Type of corrosion	Causes and observation
Uniform corrosion	Evenly corrodes the entire surface area. It will continue to thin out the surface until eventual failure [12].
Crevice	It is a form of localised attack that most often occurs in narrow fissures where oxygen access is poor and a stagnant electrolyte solution is present [13].
Pitting	Localized accelerated dissolution of metal occurs as the breakdown of passive protective film on a metal surface. One of the most dangerous corrosions among others [14].
Cavitation	Cavitation is a phenomenon in which bubble form in the low-pressure area and then collapse at metal to form pits on the metal surface [15].
Microbiologically induced	The enhancement or inhibition of corrosion happens due to the formation of a biofilm on the metal surface. Localised corrosion can lead to pinholes and leaks [16].
Stress corrosion cracking (SCC)	When a crack is subjected to tensile stress, formed due to a corrosive environment, it can lead to sudden failure even in ductile alloy metals [17].
Intergranulr cracking	An intergranular fracture happens near the boundary as the crystallised surface is more susceptible to corrosion. This occurs due to hostile environmental influence [18].
Galvanic Corrosion	When two or more metals are in contact with each other and in the presence of an electrolyte. In marine structure case, sea water. A sacrificial anode is used to prevent this kind of corrosion [19].
Erosion	As a ship constantly moves through the water, erosion happens due to chemical dissolution and mass transfer [15]

Throughout their useful lives, marine engineering structures encounter numerous security issues. These structures suffer from frequent impacts brought on by sea wind, sea waves, and dynamic working loads in addition to the harsh corrosive environment. Under the synergistic impact of the corrosive environment and cyclic stress, the corrosion fatigue crack is considerably simpler to develop than the fatigue crack in the air. The influence of environmental factors on the integrity of the marine structure is

highly dependent on the type of marine environment they are exposed. We can classify the marine environment in three parts which are shown in Table 2 [20][21].

Table 2: Marine environmental effect on the ship structure

Marine Zone	**Description of environments**	**Characteristics of steel corrosion behaviour**
Interior spaces	High humidity, higher than ambient temperature, periodic wetting possible	Only aggressive in the area where moisture can accumulate.
Atmosphere	Minute salt particles present, wind direction and velocity, rainfall, temperature, pollution, corrosion vary above the sea level etc.	The sheltered surface may deteriorate more rapidly than the surface which is exposed. Corrosion decreases with the distance from the sea.
Splash zone	(i)Wet, well-aerated surface, no fouling	(i)Most aggressive zone for corrosion in the steel. The protected coating is difficult to maintain.
	(ii) Well-oxygenated, biofouling likely to happen. Some oil pollutants from the shore may give a coating to the surface.	(ii)High corrosion for steel. However, some protection may occur due to the oil film.
Immersion	Usually submerged. Pollutants, sediment, fouling, and velocity have a role in corrosion	Biofouling restricts the flow of oxygen, which can reduce corrosion; Protective coating can also help.

Structural health monitoring (SHM) can be classified into two categories: passive and active methods. Passive SHM involves examining the structure comprehensively and measuring signals directly from operational loads or damage initiation, such as through the guided waves method, impact, or ambient

vibrations [22]. On the other hand, active SHM involves integrating sensors and actuators into the structure to excite it and measure its response [23][24]. In the case of structural members, SHM aims to detect irregularities or deformities resulting from deterioration, damage, or failure to provide information on their structural health and integrity for long-term use. To detect such deficiencies and cracks in steel structures, various innovative and non-destructive methods have been developed in current practice to assess and offer an early warning and redress for impending partial or complete structural collapse, particularly in ageing marine infrastructure [25].

2.2 NDT methods

Non-destructive testing (NDT) is a group of methods used to evaluate the properties of a material, component, or system without causing damage. NDT methods are essential in the marine industry to inspect the integrity of marine structures such as ships, offshore platforms, and underwater pipelines [26]. Non-destructive testing (NDT) is a process of testing materials without causing damage to them. This method allows inspection and evaluation of welded joints, components, or defects in welded parts without harming the material. NDT can be used to examine the quality of materials at various stages of production, including raw material, fabrication, and in-service inspection. The objective of NDT is to ensure that the material is reliable and does not fail within the expected lifespan [27]. There are various terms used to describe NDT, including non-destructive testing and non-destructive evaluation (NDE), which involve the examination and inspection of materials for irregularities, flaws, or defects. By using NDT techniques, materials with fewer defects can be selected, and the behaviour of newly manufactured materials can be studied. NDT can detect flaws that can be accepted or rejected based on established acceptance standards. Defects may include cracks, incomplete penetration, incomplete fusion, porosity, inclusions, etc., and can vary in size, type, and position. These defects pose a risk when materials are in service [28].

The capabilities and limitations of various NDT techniques are summarized in Table 3, which includes visual inspection, ultrasonic testing, magnetic particle testing, radiography testing, and liquid penetration testing.

Table 3: Various type of NDT methods

NDT technologies	Principle	Advantages	Limitation
Visual Inspection [29]	Based on Engineer/Surveyor's ability and experience, he can distinguish between different types of corrosion and cracks on the surface.	Fast and easy; a Modest skillset is required.	Only surface defects can be identified.
Ultrasonic testing [30]	The ultrasonic testing principle is based on generating and detecting mechanical waves and vibration within the sample at a high frequency of around 1 MHz to 100 MHz	Quick; deep material penetration; ideal for detecting corrosion; automatable	Contact with the sample surface and coupling media (gel or water) is needed; the Surface need to be smooth
Radiography [31]	It is based on differences in the attenuation of penetrating radiation in materials. When the corrosion is present, variation in transmitted radiation is detected.	The broad range of materials with different thicknesses can be inspected	Minimum intensity difference required; Radiation safety precaution required; Expensive.
Magnetic flux leakage [32]	It is based on leakage of magnetic flux caused by the presence of corrosion.	Portable, Inexpensive, and sensitive	Limited to ferromagnetic material;

		to corrosion on the surface and near the surface.	Surface preparation and post-inspection required
Eddy's current [33]	Holding a conducting coil with alternating currents next to the sample is the foundation of this approach. Around the coil, a primary magnetic field is created in an axial direction. In accordance with Lenz's Law, this electrical current subsequently generates a secondary magnetic field that always opposes the magnetic field of the coil. Both the magnetic field is examined using a sensor to detect the defect and corrosion.	Fast to perform; moderate cost; no probe contact required.	Limited to materials with electrically conducting; penetration depth is limited; the surface must be accessible and smooth.
Eddy's current Thermography Testing [34]	Thermography tests quantify thermal variance for a sample that has been described and reacts to a stimulus.	Good for surface corrosion; high sensitivity; remote sensing; fast; inspect the large area.	Costly; equipment must be heated and cooled; reference standards are needed; resolution on thick portions is poor.
Terahertz (THz)technology [35]	Terahertz technology is the frequency between 0.1 THz to 10 THz with the wavelength of microwave and infrared. After	Noncontact; high sensitivity; one-sided;	Costly, complicated wave interactions and

	interacting with the sample being tested, this THz wave is evaluated at or close to the radiation source. Because a discontinuity or the sample's dielectric properties would impact the THz signal, variations in the THz signal can be used to discover the inner structure of a sample.	real-time; check coating layer qualities; good resolution.	environment-sensitive
Microwave thermography [36]	The Microwave Thermography test is based on the relative thermal conductivity of corroded steel as the heat dissipates quickly in uncorroded steel.	Very sensitive, quick to complete, available time-dependent data, and able to find hidden harm.	Costly, requiring complex data processing for quantification and requiring knowledge of the affected area for localised detection.
Acoustic emission [37]	A structure responds to an external stimulus, such as a change in load, pressure, or temperature, by releasing energy that causes localised sources to coalesce into stress waves. These waves then travel to the surface, where sensors are employed to detect them.	Remote operation, Locating damage sources, operation in the hazardous zone; Non-invasive method.	Slow; Might not be able to detect the defect that grows or move; Further inspection is required.
Infrared	Infrared thermography operates	simple to use,	No information

Thermography [38]	on the basis that all objects release infrared radiation as a function of their temperature, even if it is above 0 Kelvin. The thermogram technology detects the infrared energy emitted by an object and transforms it into a temperature measurement, which is then shown as an image.	safe, non-radiative, quick to set up, and portable	on the depth or thickness of faults. Environmental factors impact the results.

2.3 Fixed structural health monitoring

2.3.1 Guided wave detection system

In the late 1880s, two brothers named Curies discovered the phenomena of piezoelectricity [39]. Piezoelectric materials working in the "direct" technique produce an electrical charge when mechanically stressed. On the other hand, when an electrical field is applied, it results in mechanical strain. In sensors like piezoelectric accelerometers, the direct piezoelectric effect is frequently used [40]. Piezoelectric materials exert localized strains and directly impact the dynamic response of the structural components when implanted or surface-bonded into a structure. Piezoelectric materials have been extensively used in structural dynamics applications due to their lightweight, robustness, affordability, and availability in various configurations, from small rectangular patches to complex geometries used to create microelectromechanical systems (MEMS) [41].

Viktorov [125], Achenbach [126], Graff [127], Rose [128], and Dieulesaint [129] studied Lamb waves thoroughly. Symmetric and anti-symmetric modes make up the two types of Lamb waves. Lamb waves and horizontal shear waves (SH) are two ways ultrasonic-guided waves travel through plates. In Lamb waves, particle motion is vertical, whereas in SH waves, it is horizontal [42]. Lamb published the first account of directed ultrasonic waves through thick plates in 1917. Both Lamb wave varieties are widely

dispersed. The decision to use Lamb waves is supported by their numerous benefits, including their ability to vibrate through the whole thickness of the plate and their ability to identify interior flaws regardless of their depth [43]. Additionally, Lamb waves can propagate in isotropic materials without suffering too much energy loss. Lamb waves can have certain drawbacks, too. Because they are disseminated at a particular frequency, many modes may propagate at various rates.

The dispersion curves have been established theoretically and experimentally validated, and the effects of dispersal over vast distances have all been studied. Various writers developed the Lamb wave propagation technique employing piezoelectric discs as the transmitter and receiver to assess the changes in the received signal from a structure bearing a defect. This technique has shown high effectiveness in finding holes, fractures, and rust in metal materials. However, many reflections have complicated signal processing. Surface waves, sometimes referred to as Rayleigh waves (R waves), are used to reduce complex signal processing. This research work centred on R wave —mechanical elastic deformation waves in solids approaching a free boundary [44]. Two parallel free limits in thin plate structural elements act as a guide for lamb waves. Unconstrained boundaries have little damping, which allows Lamb waves to propagate over long distances with little amplitude damping. Keilers and Chang [45] were the first to employ Lamb waves to identify delamination in piezoelectric materials. Then, more research was done on the wave propagation (WP) technique's for fracture identification and localization capabilities. For effective damage monitoring in thin metallic structures, researchers have looked at modelling and modifying Lamb waves [48]. The bulk of current research focuses on Lamb wave propagation in thin structures. Numerous experimental experiments have examined how Lamb waves interact with various forms of damage, including detecting impacts, fractures, and corrosion.

Surface-guided waves (R-wave) are frequently used for the wave propagation-based structural health monitoring approach. They are crucial because of their unique ability to propagate without causing significant energy loss in the materials. These characteristics make them ideal for examining pipelines,

pressure vessels, aeroplanes, ships, and bridges. The sensors can pick up the sweep sine response once the actuator produces a sweep sine signal. Cracks and corrosion in the ship's steel frame will reduce the energy of wave packets as they travel through the steel structure [46]. The system locates the damage with digital inputs from actuators and sensors, assesses its degree, and pinpoints when the transducer/structure bond has degraded.

Piezoelectric device signals can be used for damage monitoring utilizing transfer functions, time of flight analysis with a cross-correlation envelope, instantaneous baseline time reversal, and other signal processing techniques. An effective structure damage localization mapping may result from this. Surface wave excitation is anticipated when the PZT transducer is surface bonded to the surface of a steel structure (Rayleigh or R-wave). The R-wave moves through the steel's surface and rapidly shrinks in size the deeper it travels [47]. A weaker pressure wave (P-wave) with a faster velocity will also be excited simultaneously [48]. The direct piezoelectric effect transforms mechanical waves back into electrical signatures when they collide with another patch that serves as a sensor.

Echolocation is a technique used by dolphins and bats to survive in their habitats by emitting and processing signals to locate objects in front of them. This technique has been studied in depth to understand how these animals differentiate between fish and detect hidden prey. Scientists have also adopted this approach to monitor and inspect the health of structures using ultrasonic waves and guided wave geometry [56]. One of the most crucial aspects of the wave propagation approach is the actuation frequency. In transducers, the frequency of the actuation signal significantly impacts the amplitude of the recorded signal.

Many researchers investigated various actuation frequencies and eventually concluded a frequency range [54], [55]. Guided waves of around 20 kHz-25 MHz are commonly used to screen and monitor structural assets, with frequencies below 100 KHz being used for long-range screening and those above

100 kHz for high-frequency screening. When the guided wave (GW) encounters damage in the structure, it interacts with the material boundaries and surrounding media, resulting in various effects such as wave absorption, scattering, attenuation, and reflection. These effects are proportional to the severity of the damage to the structure [56]. Detecting structural damage is crucial as it can occur during manufacturing or service life due to various factors like dynamic loading, ageing, and corrosion activities, which affect the structure's strength and vibrational frequency. The steel construction fault, such as corrosion, fatigue crack, and biofouling growth, affects the wave packet's amplitude and time of flight (TOF). The TOF is the interval of time between the wave packets of the actuator and the sensor [49].

When it comes to corrosion defects, GWs are more sensitive than when it comes to fracture damage. According to the severity of the corrosion loss and variations in the group velocity of the propagated wave, the reflected portion of the signal created in cases of corrosion defects will be relatively smaller, but the TOF shift will vary [51]. To actively stimulate and detect the structure's vibrational properties, this method uses embedded or mounted piezoelectric transducers. Gao and Rose's research study [52] shows that the change in TOF results from corroded structure sections. To find sludge and corrosion buildup in pipes, the GW signal's transmitted and reflected coefficients have been employed [53].

One of the most crucial aspects of the WP approach is the actuation frequency. In transducers, the frequency of the actuation signal significantly impacts the amplitude of the recorded signal. Many researchers investigated various actuation frequencies and eventually concluded a frequency range [54], [55], [56]. There is yet to be agreement on a single ideal frequency for actuation. According to the available research, 20- 100 kHz appears to be a commonly approved frequency for isotropic material. Many studies have been carried out using the WP technique with embedded PZT transducers.

Too many to include all the uses for piezoelectric materials in structural dynamics; however, they are well covered in the literature [59]. A frequency range with several resonance peaks must be selected for

an effective damage detection technique because these peaks will alter more due to damage than a frequency range with no damage. Here, an appropriate frequency range is chosen by a trial-and-error process that involves scanning across a variety of frequency ranges [58].

Table 4: General parameter of PZT [63]

Parameter	Piezoelectric ceramic (PZT)
Piezoelectricity	High
Acoustic Impedance (10^6Kg $m^{-2}s^{-1}$)	High (30)
Density (10^3 $kg.m^{-3}$)	7.5
Relative permittivity ($\varepsilon/\varepsilon_0$)	1200
Dielectric constant	1180
Mechanical flexibility	Average
Curie temperature ($^\circ$ C)	386
Peak power (mW)	52
Volume (cm^3)	1.5
Frequency (Hz)	100

2.4 Non-destructive testing using Autonomous devices

Infrastructure inspection has made extensive use of mobile robotic technologies. In this context, there are many instances of robots designed for checking power transmission lines, dams, bridges, pipelines and sewers, aircraft skin, etc., in the robotics literature [60]. We concentrate on the contributions that are relevant to vessel inspection in the sections that follow. Numerous contributions regarding robots for vessel inspection may be found in the robotics literature. For the examination of the submerged portion of the ship's hull, many of them comprise underwater vehicles. The vehicle that Lynn and Bohlander gave as a first illustration is an underwater Remotely Operated Vehicle (ROV) designed for inspection [61]. The underwater hull's paint thickness may be measured using a special probe by this free-floating vehicle. Another remotely controlled robot with a camera suited for visual vessel inspection is the Little Benthic Crawler [62]. A commercial 2-piece robot made out of a detachable 4-wheel drive crawler skid assembly and a 5-thruster ROV. The latter has a vortex generator that exerts an attracting force on any surface that is comparatively flat. A mechanical mechanism that enables an ROV to

maintain proper orientation and position to enhance the visual examination of the hull is another example provided by Ishizu et al. (2012)[64]. AUVs have the ability to increase coverage effectiveness, increase survey accuracy, and generally lessen the requirement for human involvement. Some AUVs created for ship inspection are designed to adhere to the hull surface and crawl over it.

An underwater hull-crawling robot called the Lamp Ray provides information on the thickness, shape, and condition of hull plates. For autonomous waypoint navigation, it uses an audio beacon location system, often known as a long-baseline system (LBL). To do Non-Destructive Testing (NDT) and determine the condition of the hull, several types of probes and a non-contact underwater ultrasonic (US) thickness gauge are utilised. Up until it touches the hull surface, the vehicle may continue to function in free-swimming mode. Then, it stabilises itself using the front-mounted thrusters' suction and glides around the hull's surface on wheels, all the while the complicated geometry nearby is typically examined by a free-swimming ROV. The hull-crawling AURORA [65] underwater robot can clean a ship of marine fouling while also examining the condition of the hull using a US probe and cameras. It has two separate automatic operating modes in addition to a manual option. In the first, the robot uses vision to distinguish between regions that have previously been cleaned while estimating its direction of travel. The platform determines its relative location in the second autonomous mode by triangulating it using three US sources that are fastened to the ship's hull [66]. Similar to this, the HISMAR robotic system is designed to maintain a ship's hull that is free of biofouling in order to improve propulsion efficiency. The truck is also equipped to measure the thickness of the plates. The pilot gives control orders via an umbilical that includes power, control wires, and hoses used to deliver the cleaning wastes to the surface, much like the AURORA robot. By employing optical technologies to monitor the two-dimensional movement across the hull surface, the position is calculated via dead reckoning. Utilizing a magnetic sensor device, the absolute position estimate corrects the currently monitored location by utilising known hull properties [67].

2.4.1 Unmanned underwater vehicle

AUVs are gaining immense popularity for underwater exploration across commercial, military, and industrial domains. Numerous AUVs have been created for diverse purposes over time [68]. The conventional method of inspecting hulls underwater is through human divers conducting visual surveys. However, this is a hazardous, demanding, and time-consuming job for people, which can affect the effectiveness and accuracy of the survey results.

The exploration and development of the ocean have always been important aspects of human development. Due to the scarcity of resources, it has become necessary to strengthen ocean research and development. However, manual exploration and development in the underwater environment are extremely risky due to their harsh and complicated nature [68]. Therefore, using autonomous underwater vehicles (AUVs) for ocean research and development is a safer and more effective alternative. AUVs are also utilized in rivers, lakes, and other bodies of water.

Light behaves differently as it moves through the water, with various wavelengths of light being absorbed differently by different types of water. Red light attenuates the fastest and disappears at a depth of around 5 m underwater, whereas green and blue light attenuates more slowly and vanishes at a depth of about 60 m [69]. The direction of light changes as it propagates and scatters unevenly due to suspended particles and other media. The scattering process is influenced by the characteristics of the medium, light, and polarization. McGlamery et al. [70] provided a model for estimating underwater camera systems, which includes the input geometry, source characteristics, and optical properties of water to compute the intensity of non-scattered light, scattered light, and backscattered light. Finally, the parameters contrast, transmittance, and signal-to-noise ratio can be acquired. The traditional Jaffe-McGlamery underwater imaging model was subsequently suggested [71], which implies that the direct portion, the forward scatter component, and the backscattered component are linearly superimposed

to form the total illuminance entering the camera. The light that is immediately reflected from the surface of the item into the receiver is known as the direct irradiation component. The light that is scattered by suspended particles in water and redirected towards the receiver by a slight angle during direct propagation is referred to as the "forward scattering component." Backscattering occurs when the light is scattered by the body of water and travels to the receiver. As shown in Fig. 1 [70], light energy is often attenuated more by forward scattering than by backscattering.

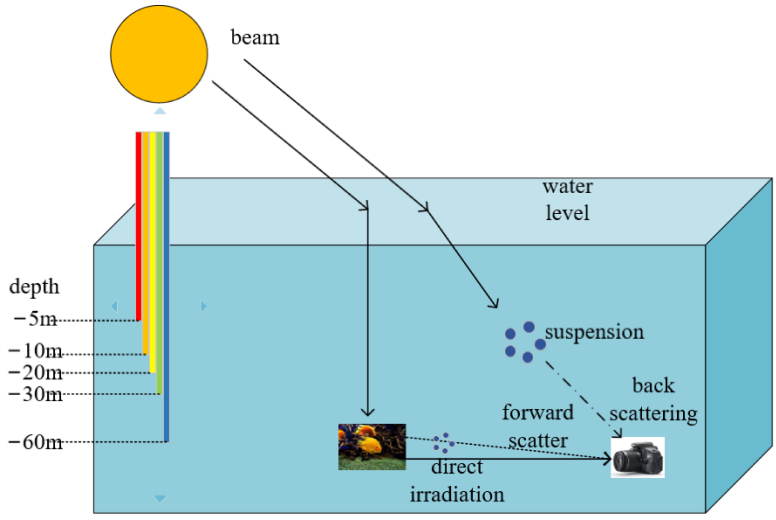

Figure 1: Forward scattering and Backscattering [70]

The video pictures captured underwater often have a blue-green appearance and an apparent fog-like effect due to the water bodies' absorption and dispersion of incoming light. The usual issues that lower the quality of underwater video pictures include blur, poor contrast, colour distortion, greater noise, indistinct details, and restricted visual range [73].

2.4.2 Unmanned ground vehicle

Even though they are often pricey, current robotic automated NDT systems can typically only check one kind of structure since they were specifically built for it. They typically have two to three Cartesian axes and can only check flat or moderately curved surfaces. There is multi-axis robot inspection equipment

with more than three axes, although they are often fixed site systems and are seldom anthropomorphic. The robot arm cannot be used for testing on buildings of diverse sizes and shapes since it moves on a monorail alongside industrial production lines or is merely fitted around a single test item with an unusual form [74]. Other systems, such as those that progress along welds around the circle of pipes, may be relocated from location to location but are still restricted in their mobility.

Magnetic crawler is fairly popular for structural inspection as ships are made of solid steel, which is conducive to using magnetic crawlers for locomotion. However, the complex geometries and obstructions on ships (such as beams, stiffeners, bolts, welds, pipes, etc.) can cause magnetic crawlers to shear off even on small obstacles. This hampers their ability to navigate the surface of ships effectively and limits their usability for ship inspection purposes. The safety issues associated with the operation of magnetic crawlers in industrial environments, such as ship hull cleaning and preparation, are also a concern. Most magnetic crawlers used in these scenarios are heavy and require cables for support to prevent damage to the robot and humans in case they shear off and fall. However, securing a robot with cables is not always feasible in certain inspection scenarios, such as when an inspector needs to inspect the top section of a tall cargo hold. To address this issue, a small, sturdy, and lightweight robot that is able to withstand a fall from several meters without endangering the surveyor and other crew members is considered [75].

2.4.3 Unmanned aerial vehicle

An unmanned aerial vehicle, or UAV, is a flying system without a pilot that typically includes control mechanisms, navigation, communication systems, and a useful payload. A UAV may perform tedious and hazardous activities as an autonomous robotic device, offering aerial access to high-risk, high-altitude locations like offshore wind turbine blades [76]. The danger of inspection duties, which often need the inspectors to operate at a high altitude, is reduced by innovation in UAV technology. UAVs can

access difficult-to-reach places because of their size and flexibility, making them useful for NDT activities like power line inspections and crack identification in bridge concrete [77]. Thus, the control method and refinement of non-contact measurement methods, such as thermographic inspections and photogrammetric, are the primary study areas in the field of UAV-based NDT currently. The other method which is considered is the hammer percussion method using UAV with a hammer to create an impact on the surface.

UAVs fitted with a high-resolution camera use photogrammetry, a kind of examination, to assess the surface quality of targeted objects. The thermographic examination focuses on tracking heat distribution to find oil or gas leaks from worn-out or damaged infrastructure, including underground pipes. These non-contact measures, however, can only detect obvious discontinuities and other noticeable surface-exposed faults. While structural health issues like sub-surface corrosion under the outer facade need contact measuring technologies, the UAV inspection procedure normally includes a reasonably significant standoff distance to prevent accidents. A close-range and touch investigation is also very difficult for the UAV pilot to carry out [78].

The other challenge faced by UAVs is settings where GPS is not available and where other external positioning systems, including motion tracking systems, cannot be implemented. Due to this, aerial platforms used for inspection typically have to estimate their state (attitude, velocity, and/or position) by utilising internal sensors and, frequently, on-board computational resources [79]. According to McAree et al. (2016), a drone inspection system that uses a LiDAR to keep a set distance and relative heading to the wall being inspected has been developed [80]. The vehicle runs in a semi-autonomous mode so that the pilot may focus on the inspection duty, and the UAV is in charge of handling the difficult task of maintaining distance without the pilot's input. The other technique which is explored by Sean et al. (2018) is the feasibility of detecting a defect in the concrete using a sounding procedure via UAV [81].

A similar initiative is carried out in other research work to detect defects using a percussion test to create a resonant flexural frequency while the hammer is mounted on the UAV [82]. The state-of-the-art and commercial use of UAVs to gather structural health data is now focused exclusively on image-based applications. Image-based applications have certain limitations, such as the fact that cleaning the surface is required to ensure good visibility of the crack. Flaws that are visible to the naked eye can be detected. Flaws under a coating, for example, are difficult to detect. These issues can be resolved using a hammer test and chain drag mounted on the UAV, as shown in fig (2) [83].

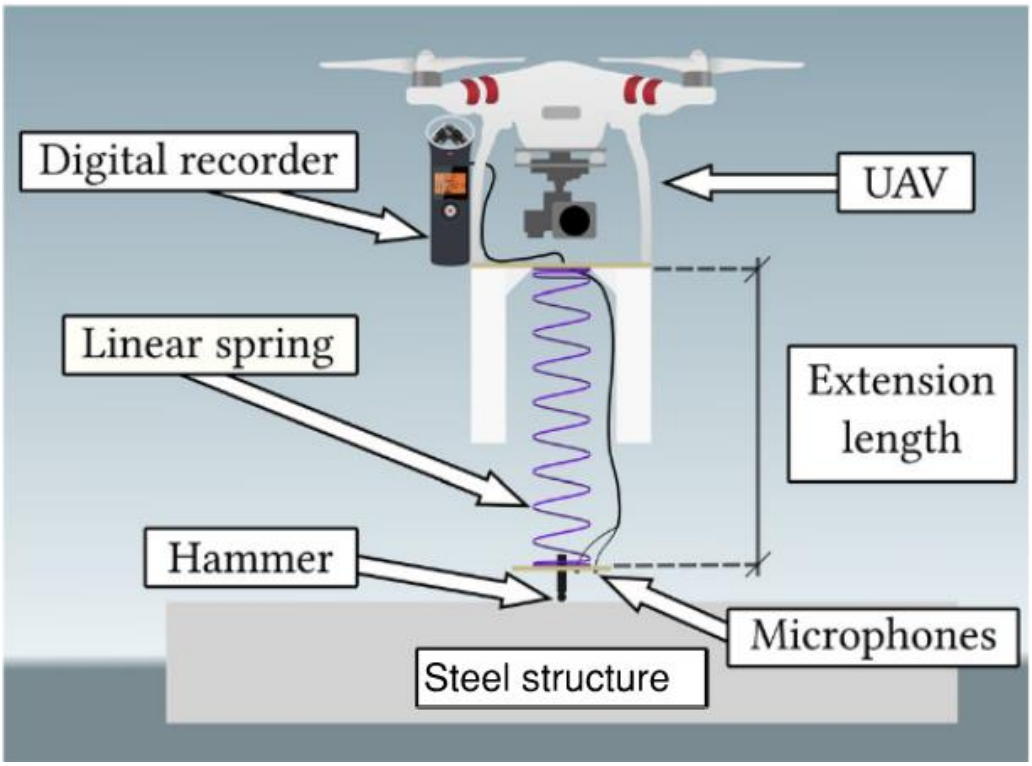

Figure 2: Overall arrangement of the hammer percussion test mounted on UAV [83]

2.5 Hammer percussion test

One of the first non-destructive testing techniques is the conventional coin-tap test, often used in laminated constructions. During percussion testing, the marine surveyor must tap a coin on each material point to be examined and then listen to the sound produced. Coin tapping cannot offer quantifiable data since it depends on the inspector's interpretation and hearing, the findings are

influenced by workplace noise, and it is vulnerable to these drawbacks. In the aircraft sector, composites are often employed. Boeing, one of the major competitors in that market, has created a digital electronic tap hammer that gives a numerical measurement of the hammer or composite impulse time that may be connected to structural faults [90].

When a component is damaged, it tends to decrease its inherent frequencies while increasing vibration damping. Since natural frequencies and damping are features that apply to the entire component, evaluating them can be an attractive non-destructive testing method. Therefore, determining the integrity of the entire component can be achieved through a single test. By striking a component, the resulting sound can be used to extract the necessary vibration qualities [84]. This formed the basis of the "wheel-tap" test used in the railroad industry [85], where a worker would evaluate the quality of a wheel's sound by listening to it. If you replace the ear of the worker with a transducer, the required properties can be calculated in seconds.

In the hammer percussion test, a straightforward, low-cost instrumented tap hammer is utilised to obtain a quantitative measurement of the hammer/steel impulse time. A link between the length of time (duration) observed with the degree of structural damage. Damage to both solid and bonded surfaces, such as the skin of an aeroplane wing, a vehicle door, a boat hull, or similar objects, may be easily located with damage-detecting equipment. The instrumented tap hammer adds a quantitative readout relating local component quality to the operator's sound discrimination. Operator variations and background disturbances have little impact on the inspection outcomes. This hammer is particularly sensitive to the local stiffness of the structure but somewhat insensitive to the size or force of the hammer impact [86]. This technique gives the test objectivity, raises the test's sensitivity, and allows the inspector to get quantitative data on the real impact reaction. The process of test carried out by Boeing [87] on their commercial airplane is as simple as an inspector making a tap in a known good area and noting or memorizing the value obtained. The inspector would then tap a questionable area and

compare the reading obtained with the reading from the good area. If the questionable area is within the acceptable range, the inspector will tap again into another suspect region until confident in mapping out the suspicious area. If it's not within the acceptable range, the suspect region may be tagged and replaced with another suspicious zone. The sound wave distinctions of the created sounds will also be difficult to identify in regions with high background noise, such as busy streets, nearby airports, industries, or building sites. While a defect's horizontal extent may be found using hammer sounding or chain dragging, its depth cannot be found using these techniques [83].

Natural frequency in this research is carried out using Fourier transform, executed through FFT, which shows that pulse duration is related to the frequency content of an impact. The amplitude spectrum plot shows that observations in the time domain correspond to observations in the frequency domain [88]. The FFT amplitude is normalized for both damaged and undamaged plots to have the same magnitude at zero frequency, allowing for assessment of the shape of the curves relative to each other. Cawley & Adams [89] developed a ratio, R, to assess the shape of the amplitude spectrum. R is the tail area fraction of the logarithmic curve to the total area under the logarithmic curve. The amplitude of the FFT for an impact over a damaged area decreases more rapidly with increasing frequency compared to an impact over a pristine area. This means that impacts over defects have less high-frequency content than impacts over good areas, resulting in a smaller value of R.

2.6 Infrared thermography (IRT) based testing

In non-destructive testing (NDT) applications, active IRT is often utilized to produce pertinent temperature differences between areas of interest by applying an external stimulus to the specimen. It is used to check materials for subsurface flaws and to find specimen sections with distinct qualities below the surface. There are several extremely modest subsurface abnormalities. As a result, the signal levels related to them may be lost in the noise of the thermographic data [91]. Different post-processing

techniques may be used in these circumstances to enhance the signal to noise ratio (SNR) content of thermographic data.

The temperature field of the body surface under study is measured and analyzed using infrared thermography during NDT [92]. The underlying theoretical idea is that the interior composition of the examined item and any faults will exhibit various thermal behaviours. A conventional design heat source will be cooled or heated at varying rates due to the flaws. The infrared camera detects variations in radiation emission as temperature changes on the surface of an object (thermal contrast). When the obtained signal is weak, data processing methods are used to the data to enhance the findings and enable flaw identification [93]. You may use NDT based on IRT utilizing a passive or active strategy. The substance under inspection must be at a specific temperature when using the passive technique. One use of this method is examining aeroplane structures to find water within panels. The active strategy is far more prevalent [94].

In active thermography, acquisition happens concurrently with applying an external stimulus to the studied object. Using a thermal contrast, the goal is to highlight subsurface abnormalities or flaws. Several stimulation techniques may be used. Most of them fall under the mechanical, inductive, or optical categories. The most typical ones rely on optical activation, which transfers energy to the specimen via light. Heat is produced by the stimulus being used, which travels through the specimen as thermal waves from the surface. Thermal waves vary their propagation rate when they encounter an anomaly, creating a thermal difference on the surface just above the anomaly [95].

Environmental factors also influence IRT measurements in a variety of ways. For example, an increased ambient air temperature results in a higher measured temperature of the objects under inquiry, but humidity, rain, or snow causes the observed temperature readings to decrease. Direct sun radiation and wind velocity both have an impact on the items' measured temperatures [96].

Studies show that in addition to emissivity, ambient temperature and relative humidity can affect the temperature of civil constructions [97]. Due to the shear effects of surface temperature, it has been observed that strong winds can make temperature monitoring of marine constructions less efficient [98]. When using IRT to monitor the temperature of the structure, it must be prevented from having standing water on the roof, Perspex, and glass components. IRT was utilized by Marinetti and Vavilov [99] to identify and characterize concealed corrosion faults in thick metallic components. The temperature difference was found to be the greatest for flaws resembling ruptured blisters when Han and Park utilized IRT to detect corrosion in steel components coated with organic material [100]. Jonsson et al. [101] and Schonberger et al. [102] also conducted related investigations. IRT has additionally been utilized to find corrosion flaws in aluminium aircraft panels. To quantify pitting corrosion flaws in iron pipes, Liu et al. used pulsed IRT techniques [103].

Principal component analysis and phase congruency measurement was carried out, and it was found that the second principal component has a linear connection with the material loss. According to studies [104], IRT-based approaches can only achieve an acceptable degree of accuracy when there is at least a 20% loss in wall thickness owing to corrosion. Hermanson and Sandor [105] showed how forced diffusion thermography and a frame subtraction-based image processing approach could be used to simulate corrosion fatigue. The rate of temperature rise was found to increase with the level of corrosion in reinforced bars when Chung et al. employed IRT to measure corrosion in those bars [106]. In high-temperature pipelines, which are most frequently used in petrochemical industries and power plants, Shen and Li discovered that IRT is a powerful tool for identifying corrosion pits and wall loss faults [107]. According to their investigations, IRT could quickly find corrosion faults with a depth of 40% and a wall thickness of more than 10%. Corrosion-induced flaws shorten the service life of components, and IRT-based non-contact condition monitoring estimates material loss due to corrosion and so aids in determining the components' remaining life [108].

3 Methodology:

3.1 Hammer percussion test:

In hammer percussion testing, a microphone is used to record the acoustic response, while steel specimens are struck with a hammer to cause an acoustic disturbance. The specimens are placed on a sponge pad to simulate resonance frequency when struck by a hammer. A 56.7-g (2-ounce) steel ball hammer is used, and the resulting acoustic response was recorded using a set of microphones and an audio recorder, as shown in fig(3). The Zoom H1 digital voice recorder was used to record the audio. With a maximum sampling rate of 96 kHz at 24-bit depth, this recorder is capable of recording vibration frequencies up to 48 kHz. Additionally, Zoom H1 has a 24-bit depth analogue-to-digital conversion capability, ensuring great precision during post-production. A Polsen OLM-20 Dual Omnidirectional Lavalier Microphone was utilised. The distance between the microphone and the specimen is kept between 5 to 25 mm to reduce environmental noises [109]; in addition, as the microphone has two channels, the closest channel to the surface of the specimen was utilised for post-processing. The acoustic data were trimmed using Audacity® audio software to get rid of the ambient noises that were recorded before and after the hammer hit. MATLAB© was used to perform Fast Fourier transformation on the WAV file, and the peaks are identified as the resonant frequency. Any particular specimen has various resonant frequency modes. The total number of specimen used in this experiment are 8 steel ring. Out of 8 rings, four steel rings have a bigger outer diameter(OD), and four steel rings have smaller outer diameters (OD) with different thicknesses, which can be used to simulate various marine structures such as underwater pipe, offshore structures and ship hull. The dimension of all the specimens used is given in the following table 3.

Table 5: Properties of the specimen and dimension

Outer diameter	Inner diameter	Material
455.5	400	Mild steel
235	210	Mild steel

For a ship with a length between 163.5 m to 401 m, the nominal thickness range for the hull is somewhere between 12.7 mm and 35 mm [110]. The big and small steel ring has material properties as well as thickness similar to the actual thickness of the ship hull. That's why the results on the specimen will be equivalent on the marine structure as long as we can ensure the testing condition is met. The underwater steel pipe has a thickness depending on the depth of the water, type of cargo and environment; thus, it ranges from 12.4 mm to 72 mm [111].

Figure 3: Hammer percussion test equipment

3.2 Wave propagation test using Piezo patches:

Figure (4) show the piezo patches attached to specimens using bonding material. The piezo patches P1 is used as an actuator, and the P2 is used as a sensor for detecting the harmonic signal. To approximate a corrosion-type damage, a rectangular notch was employed for simplicity. A rectangular notch could be a first-step approximation of a corrosion type defect, which is frequently utilised in lab experiments and theoretical research [121]-[124], despite the fact that a real corrosion defect may have rough, unpredictable surface characteristics.

In this experiment, a Harmonic signal is generated using the RIGOL DG1022 function/arbitrary waveform generator. The signal from the waveform generator is amplified by using the PI piezo power amplifier (Model E-413.D2) before triggering the piezo patch P1. The harmonic response signal of the P2 piezoelectric sensor is recorded by using the Tektronix digital oscilloscope (Model TBS 1064). The Tektronix oscilloscope is also used to record the signal from the P1 actuator to calculate the time delay for the harmonic signal to reach the P2 sensor. The piezopatches is glued to the steel plate for proper contact with the steel plate and steel ring. The below figure (5) shows the complete setup as well as complete details.

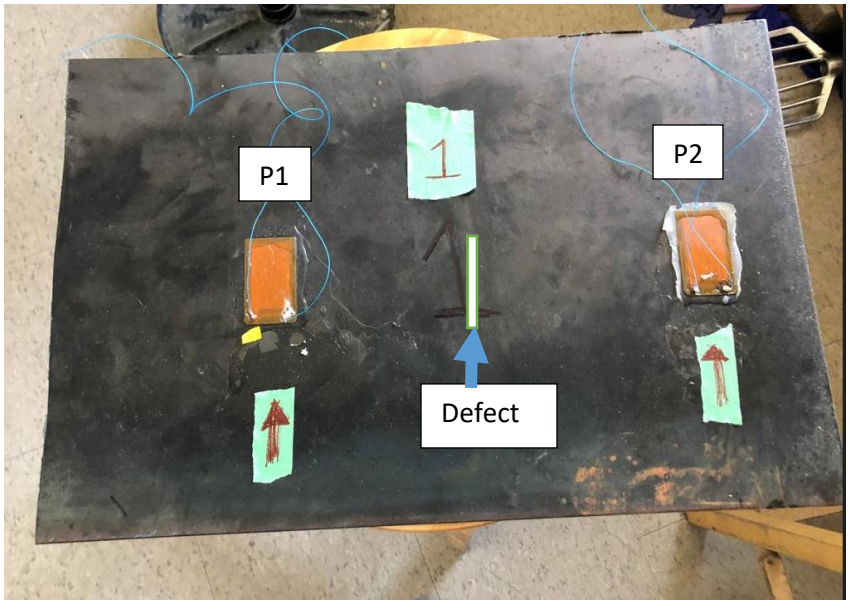

Figure 4: Steel testing plate with the piezo patch attached with adhesive

For the sake of simplicity, corrosion-type damage [113]-[114] was approximated by making a cut with the grinder to form a rectangular notch. Initially, the dimension of the defect is kept at 70 mm in length, 3 mm in width and 1 mm deep, and subsequently, it is increased to monitor the harmonic response. The rectangular notch depth and width are increased slowly to observe the response of the harmonic wave, as shown in figure (5). Table 5 depicts the material property specimen used for the experiment[125]. The high-frequency sine wave activates the actuator P1. The amplitude of the recorded signal at the sensor varies significantly based on the actuation frequency. Rayleigh wave is used to detect discontinuities such as a notch in a plate and ring. The reflection and transmission coefficients of the scattered field were evaluated considering the profiles of the discontinuity [112]. As discussed earlier, various researchers kept the frequency between 20 and 100 kHz for detection of the defect. In this experiment, the frequency response is kept at 55 kHz, which is considered acceptable as it falls in the acceptable range.

Waveform Signal generator

Oscilloscope

Wave output

Harmonic wave

Amplified signal

Piezo Amplifier

Test Specimen

Figure 5: Piezo patches based experimental set up

One of the key components of the Wave propagation technique is the actuation frequency. The frequency response was observed between 50 KHz and 62 KHz. The two specimens are tested 1) Flat steel plate and 2) Thick steel ring. The specimen dimension can be seen in the figure (6).

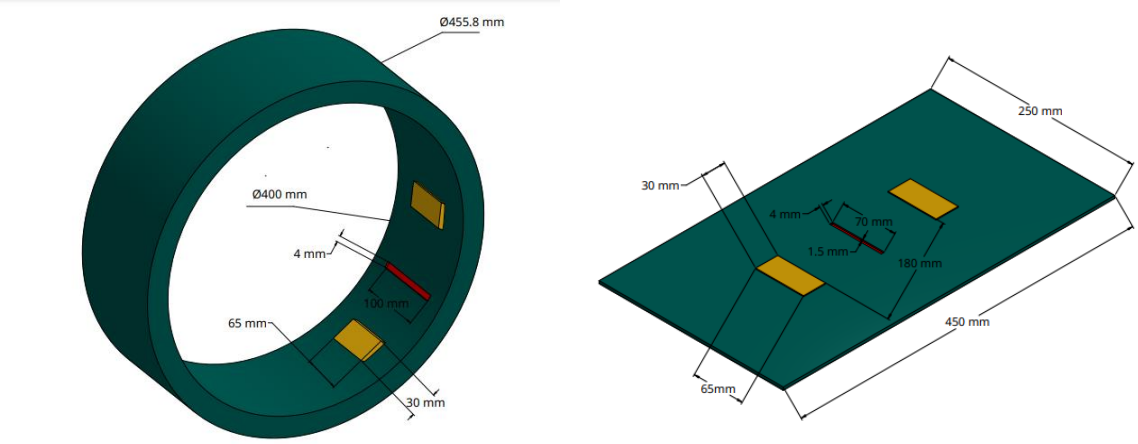

Figure 6: Specimens for Experiment

3.3 Infrared-based testing:

Infrared thermography is effective for composite and thin metal to detect cracks, but for thick metal, it can only detect surface cracks. To identify the surface of diverse specimens undergoing NDT testing, infrared thermography is used. Using a FLIR SC5000 infrared camera, a surface flaw was found. This camera has an indium tin oxide (InSb) detector with a 320 by 256 element array that is cooled using a Stirling cycle. The temperature is better than 25 mK, and the spectral range is 2.0-5.1 m. The camera was kept fairly close to the samples so that the axis of the camera and the samples were parallel to one another for taking clear detection of the crack.

4 Results:

4.1 For hammer percussion testing and chain drag attached to the drone

Hammer percussion test:

The kind of material and its dimensions affect the resonance frequency of the material. Corrosion and fatigue cracks have a significant impact on it as well. To assess the resonance frequency response, a sample with a flaw is used. The frequency response of the sample with the fault and the sample without the flaw is strikingly similar up to mode five of the resonance frequency, as was observed during testing. However, all 100 readings between the material with the flaw and the material without the defect indicate a consistent deflection of approximately 30 Hz, as indicated in appendix B; the deflection can only be seen at Mode 6 of the resonance frequency. The size of the defect is as small as 2mm deep,5mm long and 2mm wide.

The resonance frequency of a cylindrical tube can be determined using the following equation:

$$f = (m/2L) * \text{sqrt}(E/\rho) \quad (1)$$

Where f is the resonance frequency, m is the mode number (1, 2, 3, etc.), L is the length of the tube, E is Young's modulus of the material, and ρ is the density of the material [115].

To determine the resonance frequency using FFT, frequency analysis is performed on the vibrations of the tube. This can be done using an accelerometer or other vibration measurement device. In our case, the sound is recorded over the microphone. The FFT algorithm can then be used to convert the time-domain signal into the frequency domain, where the resonance frequency can be identified as the peak frequency in the spectrum.

It's worth noting that the equation 1 assumes that the ends of the cylindrical tube are completely free to move, which may not be the case in all situations. Additionally, the actual resonance frequency may be

affected by other factors, such as the wall thickness of the tube, the presence of any internal structures or obstructions, and the boundary conditions at the ends of the tube.

4.2 For Piezo patches using surface-guided wave

The difference in time between the wave's generation at the actuator and reception at the sensor is known as the time of flight (TOF). Cross-correlation analyses are carried out to determine the TOF signal. Cross-correlation is a useful tool for effectively calculating the similarity between the two sets. The TOF of the wave signal is computed using MATLAB software. The graph below demonstrates the tallest peak, which indicates the wave's arrival time. The velocity is calculated based on the time delay and the distance between the actuator and the sensor. To get the mean velocity, the average of 10 velocities is determined. The velocity of wave propagation without the defect is almost 8-10 times higher than that of the velocity with the defect. Due to the defect, the velocity of wave propagation was reduced, and it took more time to reach the sensor. The drop in wave velocity can serve as an ideal indicator for employing piezoelectric patches to find cracks and defects. The mathematic formula for the co-relation is as follows [114][116]:

$$p_{12}(j) = \frac{\frac{1}{N}\sum_{n=0}^{N-1} x_1(n)x_2(n+j)}{\frac{1}{N}[\sum_{n=0}^{N-1} x_1^2(n)\sum_{n=0}^{N-1} x_2^2(n)]^{\frac{1}{2}}} \quad (2)$$

where p12(j)= cross correlation coefficient , n= Point of reference , N=Total number of point, x1(n)= data sequence 1, x2(n) = data sequence 2, j= the amount of lag.

The cross-correlation approach is used by the MATLAB programme to calculate the TOF for this experiment. Figure(6) shows the typical cross-correlation curve between the sensing and actuating characteristics. By locating the cross-correlation distribution's highest value, the TOF can be precisely determined.

To calculate the distance that waves must travel from the actuator to the sensor, the distance between the two sensors is measured using a scale. The wave's velocity is calculated based on the distance it covers throughout its trip. When there is a route defect, which can be seen by numerous observations, the wave's velocity varies. The result can and graph can be found in Appendix A.

4.3 For Infrared signal processing

According to Dorafshan et al. [117, 118], cracks appear as hot spots or regions on the thermal camera when the outside temperature is lower than the object temperature. In contrast, cracks would appear as cold patches if the area of interest was colder than the surroundings. The cracks can be distinguished because it is cooler than the surroundings 6 (a)(b). Generally, steel plate surfaces in field equipment are frequently covered in oxide coatings, oil stains, and corrosion residue owing to prolonged exposure to oxygen and storage conditions. These occurrences will significantly alter the emissivity of the steel plate surface. Hence the clear cracks might be hard to observe in the field study using a passive monitoring approach. Also, as mentioned earlier, the angle at which the photos are taken also plays a significant role in the detection of the crack. Detection done more than 1 m away give ambiguous results to detect small scratch of 2 mm deep and 10 mm wide, as shown in fig. 7 (c).

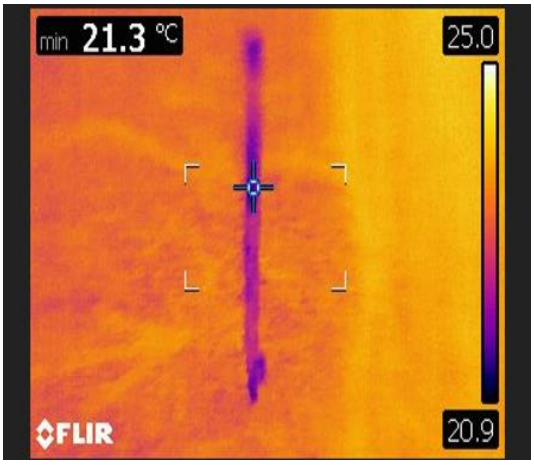

Fig. 7(a)

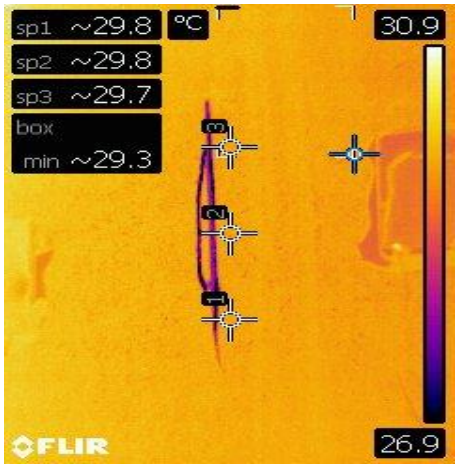

:

Fig. 7 (b)

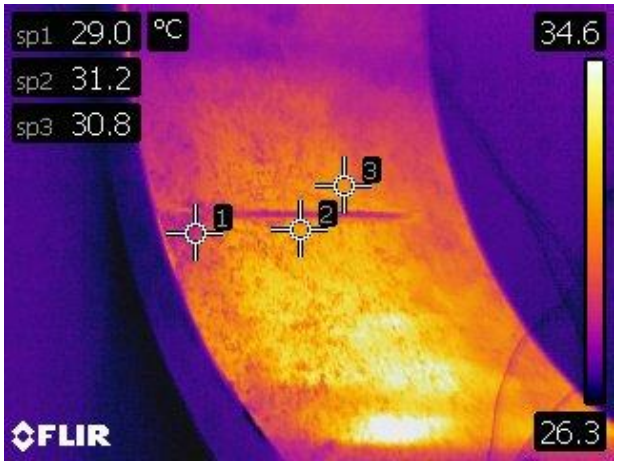

Fig. 7 (c)

4.4.Comparison

The introduction of smart materials such as piezoelectric (PZT) transducers has a major impact on the field of Structural health monitoring based on the non-destructive testing (NDT) method. A lot of literature reviews and experiments are carried out for monitoring the health of the ship hull structure by

using the remote autonomous vehicle, but less attention is given to fixed continuous health monitoring systems. This is due to certain limitations of this sensor in monitoring the range of area and relatively higher cost. The range of the PZT reduces if a lot of obstruction or bulkhead is present in the path of the travelling wave. This can be one of the reasons it is not popularised. However, the PZT-based monitoring system is very efficient in finding subsurface defects, as shown in Appendix A. It can detect surface defects as small as 7 mm by 2 mm. It still has limitations with the amount of area it needs to cover, even if the price of the PZT transducer goes down.

An unmanned aerial vehicle using hammer percussion test and infrared testing can address the problem of the amount of area that needs to be covered for visual inspection as well as placing of the piezo patches.

5 Conclusion

In conclusion, it can be argued that a single solution won't be the ideal way to do away with the necessity of surveyors manually conducting the field survey. Installing piezo patches in locations where corrosion and defects are more frequent, such as the splash zone, midship, and front of the ship, makes the piezoelectric solution an effective way of SHM. Similar parts of the ship that are vulnerable to heavy loads or bad weather can be identified. The continual monitoring of this area is crucial, and in high-fatigue failure zones, SHM systems based on piezoelectric patches can be employed. Hammer percussion testing can be extremely dependable in places like cargo holds and ballast tanks that are somewhat hard to access and where eye inspection is not very reliable. Drone-mounted hammer percussion testing can be transported to dangerous and inaccessible sites. Earlier non-destructive testing techniques offer a large area for problem location. The crack or corrosion can be identified at its precise location using infrared thermography mounted on UAV. The infrared camera can identify the

corrosion and crack because their thermal signatures differ from those of the surrounding area. As a result, it is possible to achieve complete ship health monitoring by combining all three methods.

A. Appendix A

A.1 Shrink Ring as a specimen

Figure A.1.1: Steel ring with Piezo Patches

Table A.1.1: Dimension of the Steel Ring

Parameter of the steel ring	Dimension (mm)
Thickness	27.94
Width	152.5
Inner diameter	400
Outer diameter	455.8

Table A.1.2: Dimension of the defect in the Steel ring

Defect parameter	Dimension (mm)
depth	1-2 mm
length	100mm
Width	4mm

Table A.1.3: Steel Ring with defect velocity calculated using TOF

Sr. No.	Time difference between the actuator and sensor	Velocity (m/s)
1	3.5e-4	742.851
2	3.4e-4	764.21

3	3.3e-4	787.87
4	3.6e-4	722.27
5	3.5e-4	742.85
6	3.3e-4	787.87
7	3.5e-4	742.85
8	3.5e-4	742.85
9	3.4e-4	764.70
10	3.5e-4	742.85
11	3.6e-4	722.27
12	3.6e-4	722.27
13	3.5e-4	742.8
14	3.5e-4	743.7
15	3.3e-4	787.3
16	3.5e-4	742.8
17	3.5e-4	742.6
18	3.3e-4	787.8
19	3.5e-4	742.8
20	3.5e-4	742.8
21	3.6e-4	722.4
22	3.6e-4	722.2
23	36e-4	722.2
24	3.5e-4	742.8
25	3.4e-4	764.2
26	3.5e-4	742.8
27	9.7e-4	268.4
28	1.1e-3	245.8
29	1.1e-3	247.4
30	9.8e-4	265.3
31	9.7e-4	268
32	1.1e-3	247.6
33	9.8e-4	265.1
34	1.1e-3	247.1
35	1.1e-3	247.6
36	1.1e-3	247.6
37	9.8e-4	265.6
38	1.1e-3	247.6
39	1.1e-03	247.6
40	1.1e-03	245.3
41	9.8e-4	265.6
42	1.1e-03	245.3
43	9.7e-4	268
44	1.1e-03	265.2
45	1.1e-03	245.3
46	3.5e-4	742.8
47	1.1e-3	245.8

48	3.6e-4	722.2
49	36e-4	722.2
50	1.1e-03	247.1
	Mean value=7.7 E-04 sec	**Mean value =539.20822 m/s**

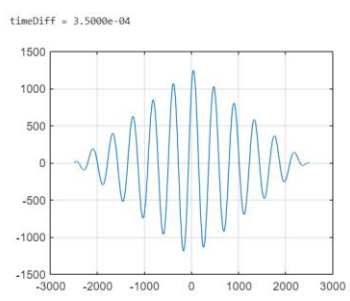

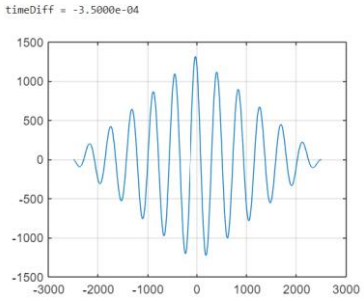

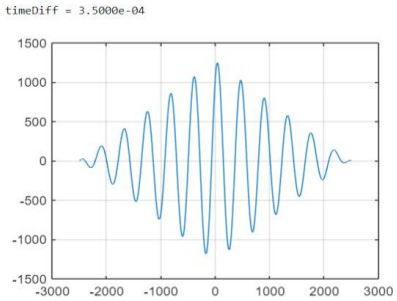

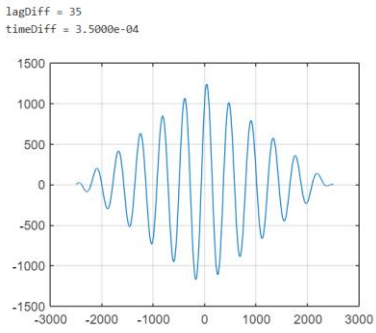

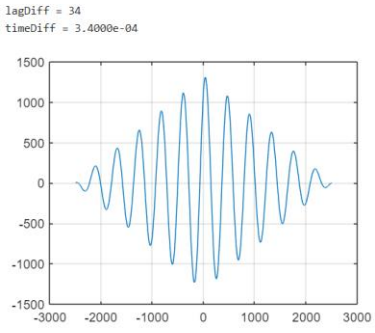

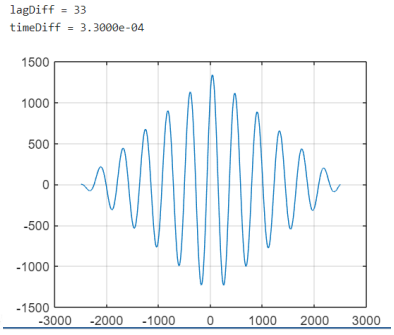

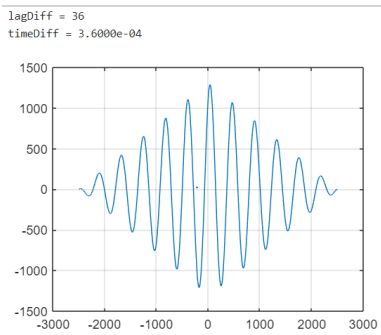

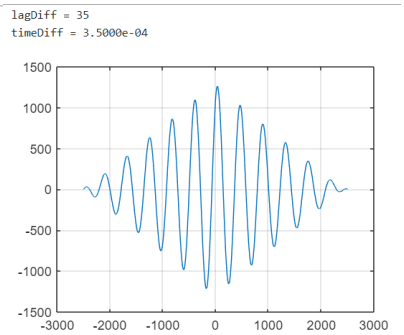

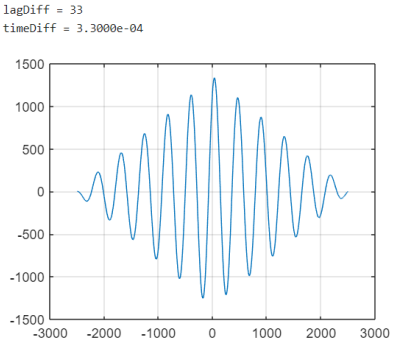

lagDiff = 35
timeDiff = 3.5000e-04

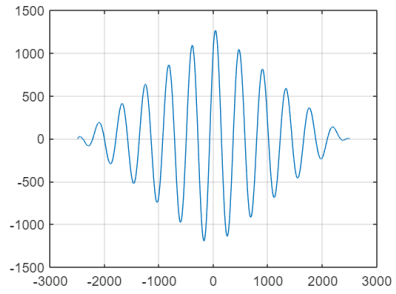

lagDiff = 35
timeDiff = 3.5000e-04

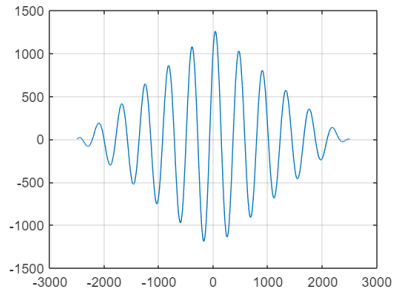

lagDiff = 34
timeDiff = 3.4000e-04

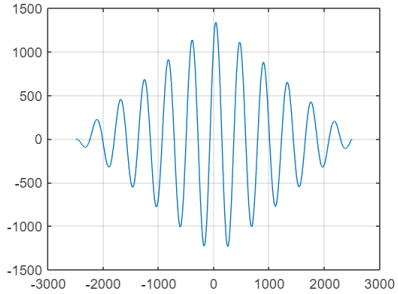

lagDiff = 35
timeDiff = 3.5000e-04

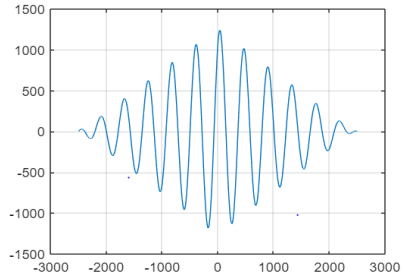

lagDiff = 36
timeDiff = 3.6000e-04

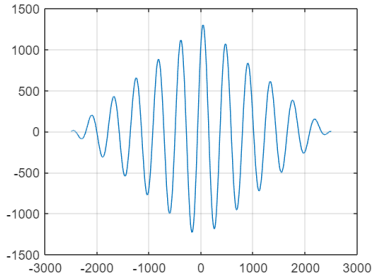

lagDiff = 36
timeDiff = 3.6000e-04

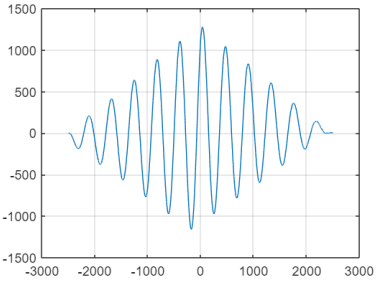

timeDiff = -3.5000e-04

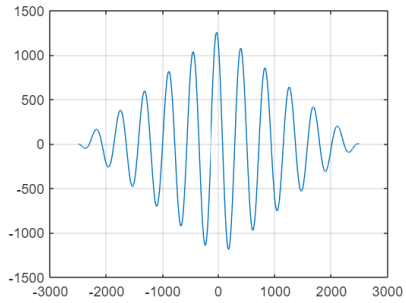

timeDiff = 3.5000e-04

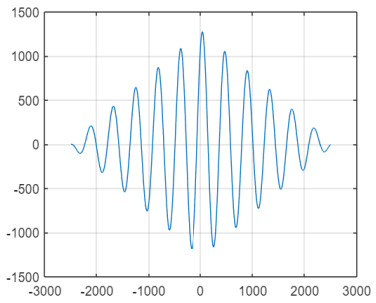

timeDiff = 3.6000e-04

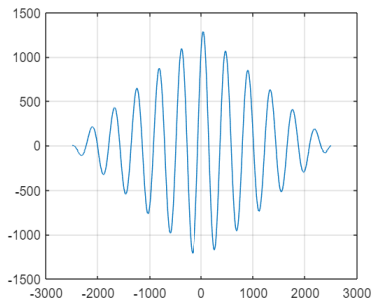

timeDiff = 3.5000e-04

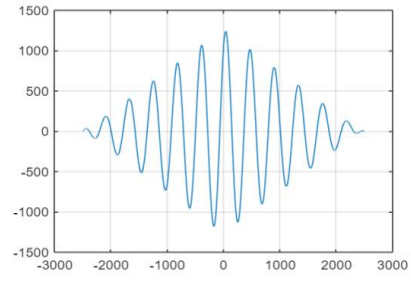

lagDiff = 34
timeDiff = 3.4000e-04

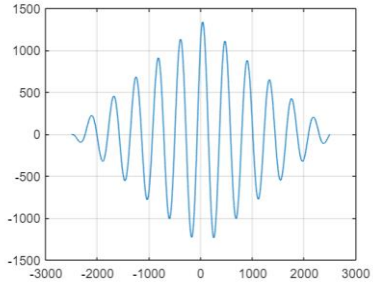

timeDiff = -9.7000e-04

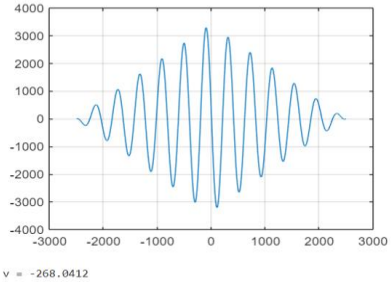

v = -268.0412

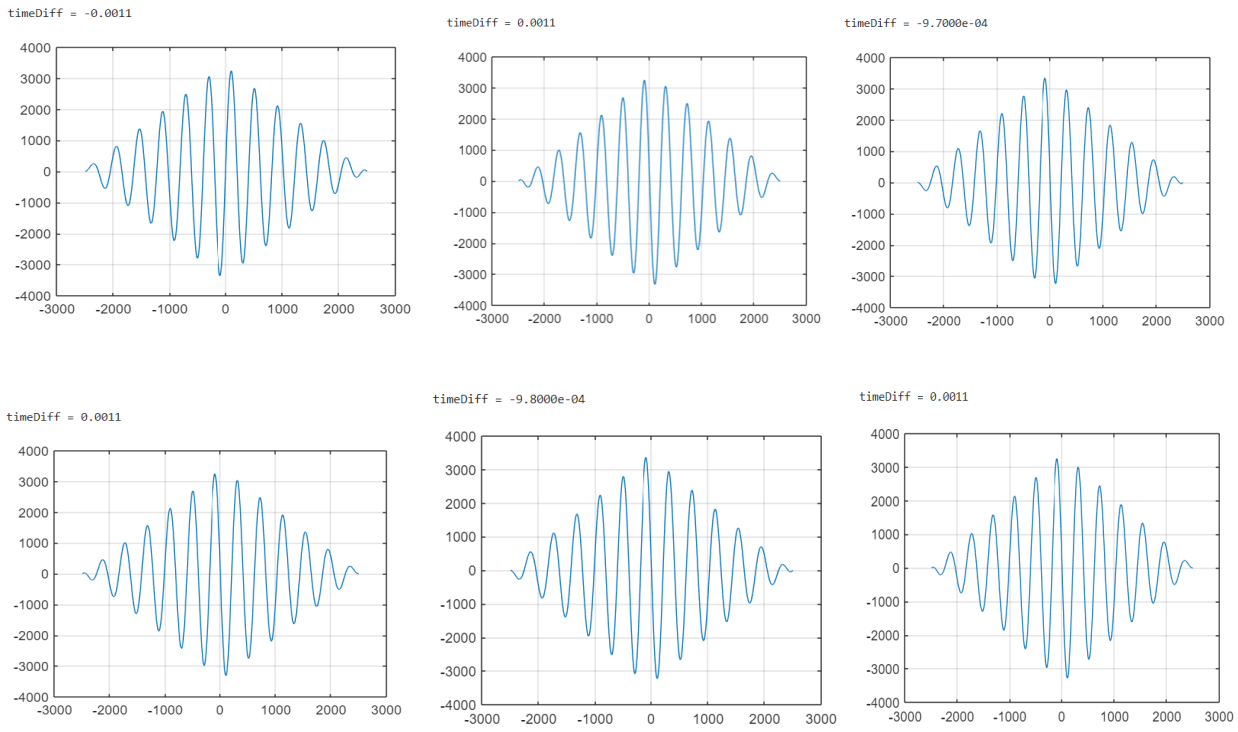

Figure A.1.2: MATLAB results for Steel ring with defect

Table A.1.4: Steel ring without defect velocity calculate using TOF

Sr. No.	Time difference between the actuator and sensor	Velocity (m/s)
1	9.0e-05	2.889e+3
2	7.0e-05	3.714e+3
3	9.0e-05	2.889e+3
4	6.0e-05	4.333e+3
5	6.0e-05	4.333e+3
6	6.0e-05	4.333e+3
7	9.0e-05	2.889e+3
8	5.0e-05	5200
9	5.0e-05	5200
10	6.0e-05	5850
11	7.0e-05	3.714e+3
12	9.0e-05	2.889e+3
13	6.0e-05	4.333e+3
14	6.0e-05	4.333e+3
15	6.0e-05	4.333e+3

16	9.0e-05	2.889e+3
17	5.0e-05	5200
18	0	5850
19	0	5850
20	0	5850
21	7.0e-05	3.714e+3
22	9.0e-05	2.889e+3
23	6.0e-05	4.333e+3
24	6.0e-05	4.333e+3
25	6.0e-05	4.333e+3
26	7.0e-05	3.714e+3
27	9.0e-05	2.889e+3
28	7.0e-05	3.714e+3
29	9.0e-05	2.889e+3
30	6.0e-05	4.333e+3
31	5.0e-05	5200
32	5.0e-05	5200
33	5.0e-05	5200
34	5.0e-05	5200
35	5.0e-05	5200
36	5.0e-05	5200
37	7.0e-05	3.714e+3
38	9.0e-05	2.889e+3
39	6.0e-05	4.333e+3
40	6.0e-05	4.333e+3
41	5.0e-05	5200
42	5.0e-05	5200
43	5.0e-05	5200
44	7.0e-05	3.714e+3
45	9.0e-05	2.889e+3
46	5.0e-05	5200
47	5.0e-05	5200
48	9.0e-05	2.889e+3
49	7.0e-05	3.714e+3
50	0	5850
	Mean value= 4.64E-05 sec	**Mean value =4.1E+03 m/s**

timeDiff = 9.0000e-05

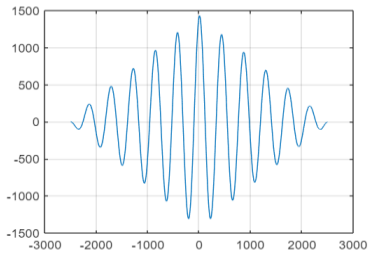

timeDiff = 7.0000e-05

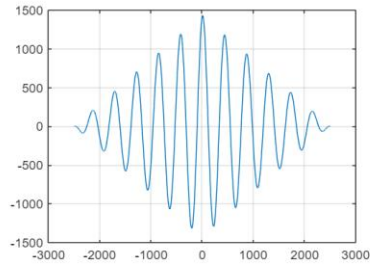

timeDiff = 6.0000e-05

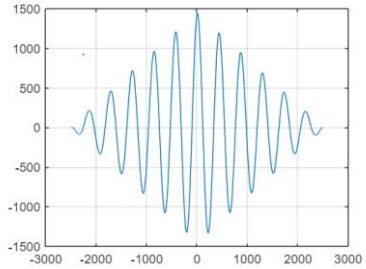

timeDiff = -6.0000e-05

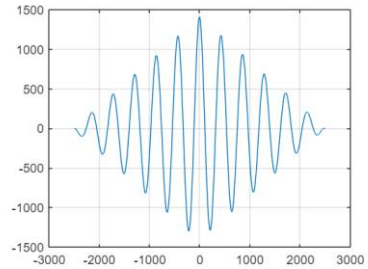

timeDiff = -5.0000e-05

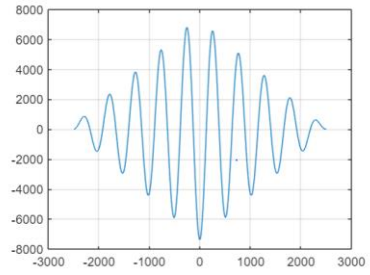

timeDiff = 0

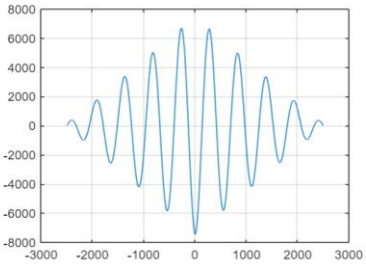

lagDiff = 0
timeDiff = 0

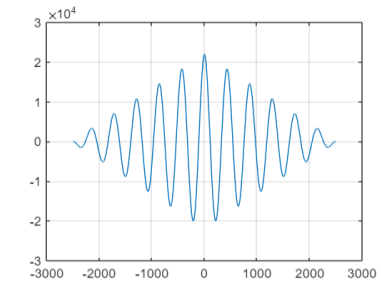

lagDiff = 0
timeDiff = 0

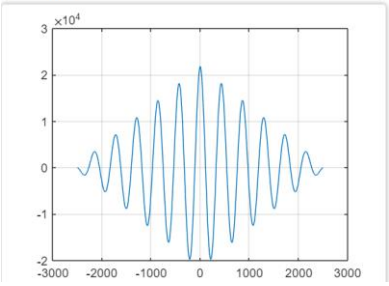

lagDiff = 0
timeDiff = 0

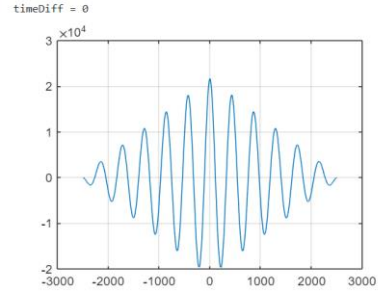

lagDiff = 0
timeDiff = 0

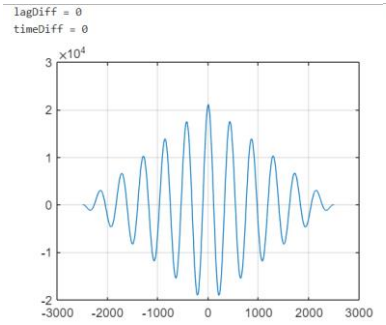

lagDiff = 0
timeDiff = 0

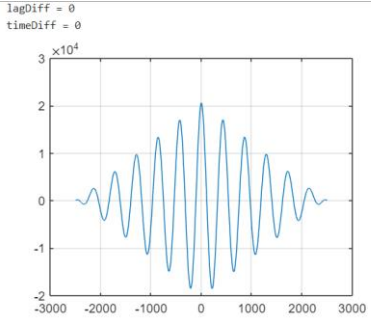

lagDiff = 0
timeDiff = 0

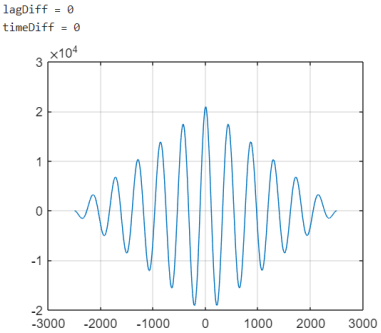

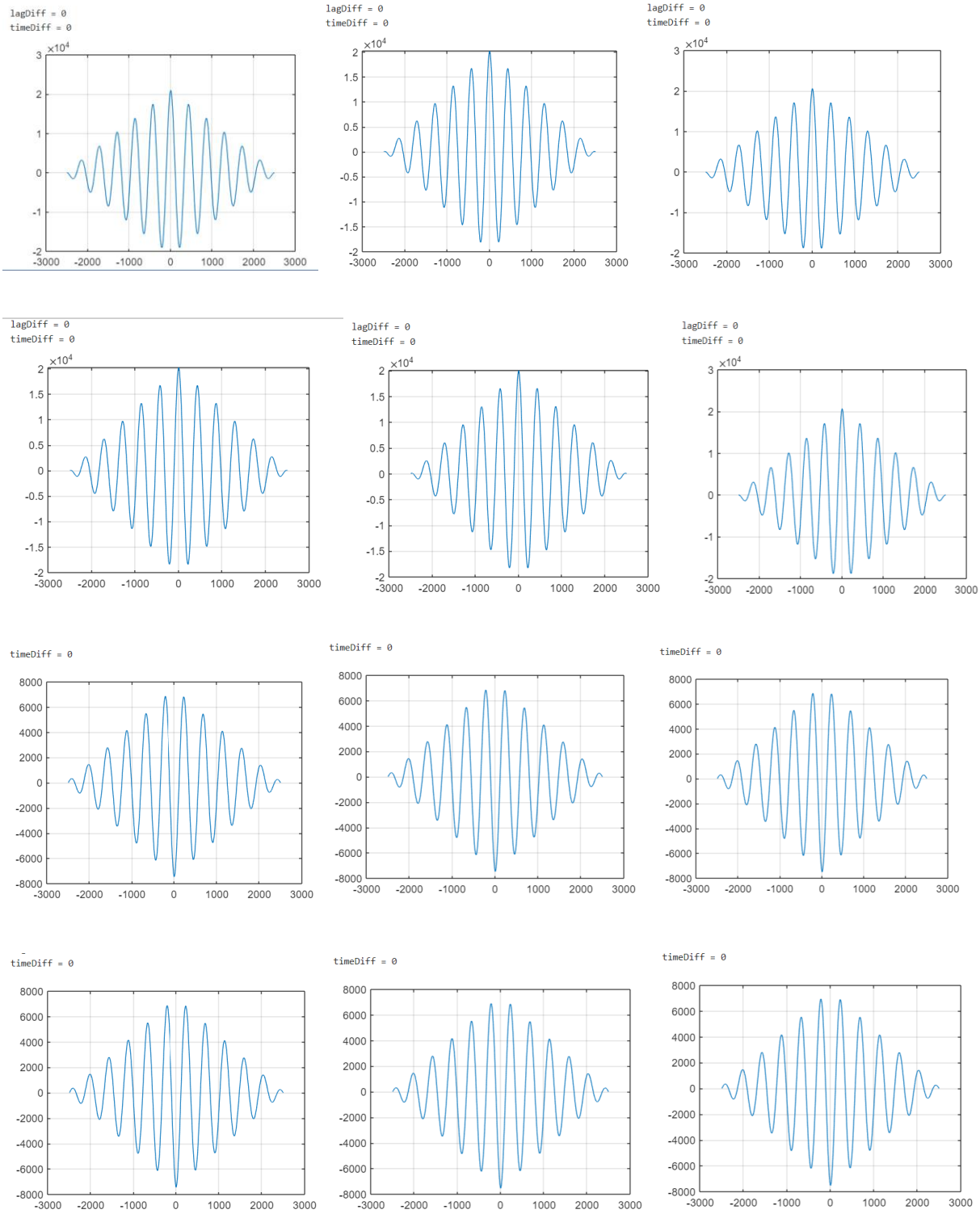

Figure A.1.2: MATLAB result for Steel ring without defect

A.2 Steel plate as a specimen

Figure A.2.1: Steel plate as a Specimen

Table A.2.1: Dimension of the steel Plate

Parameters	**Dimension (mm)**
Thickness	3.45 mm
Length	200 mm
Width	132.5 mm

Table A.2.2: Dimension of the Defect in the steel plate

Defect parameter	**Dimension (mm)**
Depth	1-2mm
Length	70 mm
width	4 mm

Table A.2.3: Steel Plate without defect velocity calculate using TOF

Sr. No	The time delay between Actuator and Sensor (sec)	Velocity (m/s)
1	1.0e-04	2600
2	0	5850
3	0	5850
4	9.0e-05	2888.9
5	1.0e-04	2600
6	1.0e-04	2600
7	9.0e-05	2888.9
8	1.0e-04	2600
9	5.0e-05	5200
10	0	5850
11	1.5e-04	1733
12	1.6e-04	1650
13	1.3e-04	2000
14	1.6e-04	1625
15	1.3e-04	2000
16	1.3e-04	2000
17	1.5e-04	1733
18	1.2e-04	2167
19	1.4e-04	1857
20	1.2e-04	2167
21	1.2e-04	2167
22	8.0e-05	3250
23	1.2e-05	2167
24	9.0e-05	2888
25	1.1e-04	2363
26	1.1e-04	2363
27	1.2e-04	2167
28	9.0-e05	2887
29	8.0-e05	3250
30	1.1-e04	2363
31	7.0-e05	3714
32	1.1-e04	2363
33	1.1-e04	2363
34	1.1-e04	2365
35	1.1-e04	2365
36	1.1-e04	2365
37	8.0-e05	3250
38	7.0e-05	3714
39	8.0e-05	3250
40	1.1e-04	2367
41	9.0e-05	2888
42	8.0e-05	3250

43	1.0e-04	2650
44	1.0e-04	2600
45	7.0e-05	3714
46	1.2e-04	2167
47	8.0e-05	3250
48	1.0e-04	2650
49	8.0e-05	3250
50	1.1-e04	2363
	Mean the value =7.47E-05 sec	**Mean velocity= 2820 m/s**

lagDiff = 1
timeDiff = 1.0000e-09

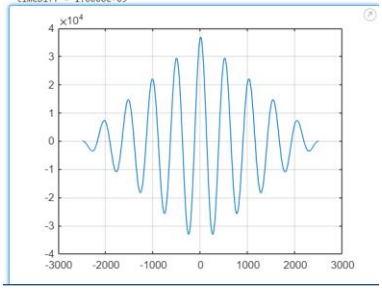

lagDiff = 0
timeDiff = 0

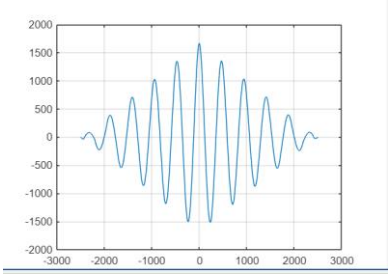

lagDiff = 0
timeDiff = 0

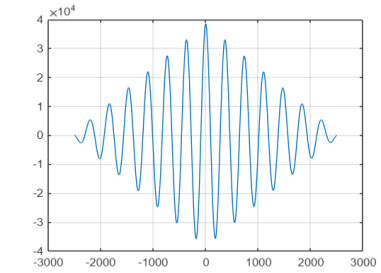

lagDiff = 9
timeDiff = 9.0000e-09

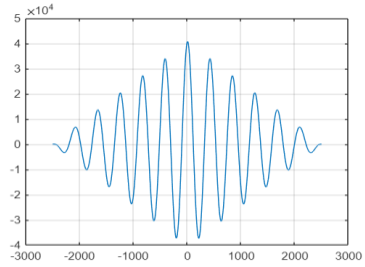

lagDiff = 1
timeDiff = 1.0000e-09

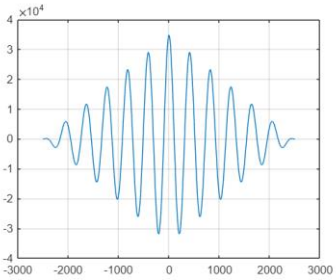

lagDiff = 1
timeDiff = 1.0000e-09

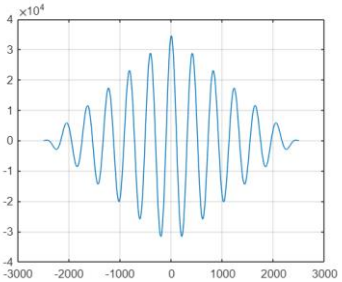

lagDiff = 9
timeDiff = 9.0000e-09

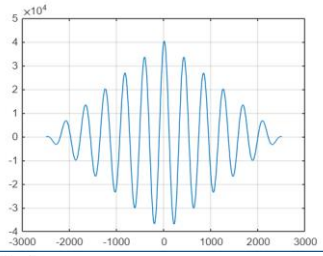

lagDiff = 1
timeDiff = 1.0000e-09

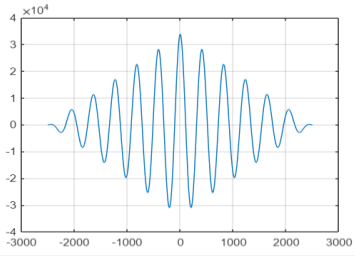

lagDiff = 5
timeDiff = 5.0000e-09

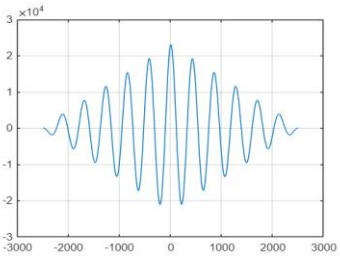

lagDiff = 0
timeDiff = 0

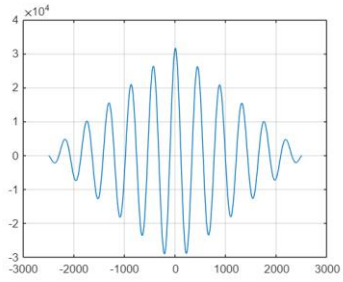

timeDiff = 1.5000e-04

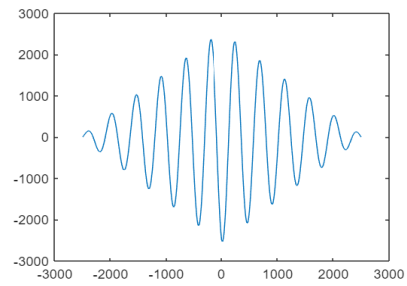

timeDiff = 1.6000e-04

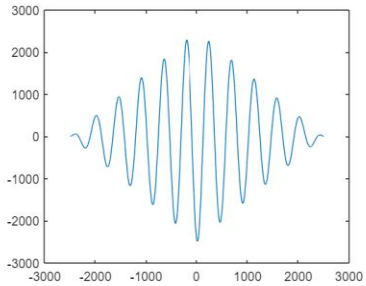

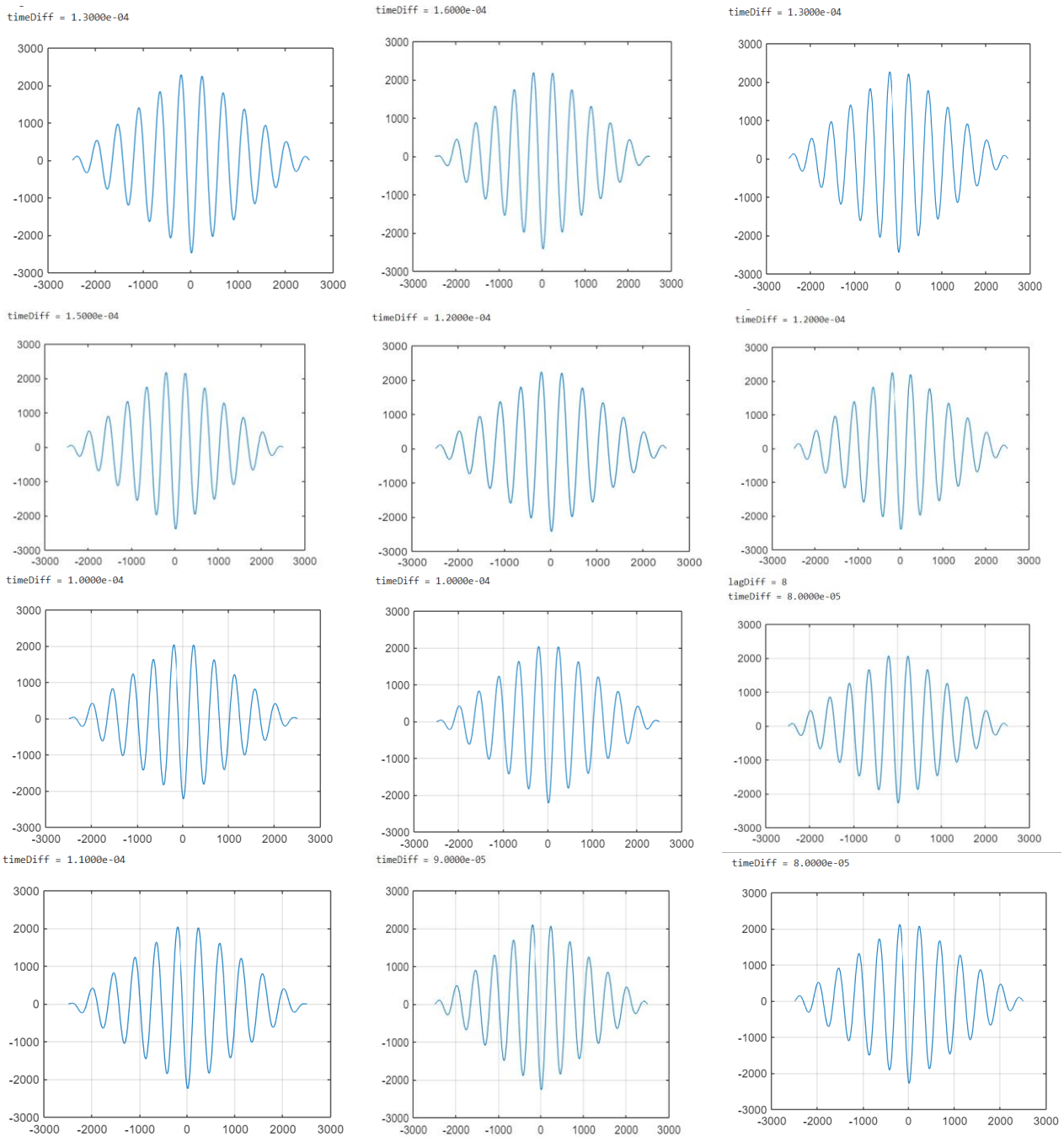

Figure A.2.2: Matlab result for Steel plate without defect using TOF

Table A.2.4: ***Steel Plate with defect velocity calculate using TOF***

Sr. No	The time delay between Actuator and Sensor(sec)	Velocity (m/s)
1	1.4e-03	192.5
2	1.1e-03	236.3
3	8.8e-04	295.4
4	9.0e-04	288.9
5	1.35e-03	192.5
6	9.0e-04	288.9
7	1.9e-03	136.8
8	1.9e-03	136.8
9	1.6e-03	162.5
10	1.6e-03	165.0
11	6.8e-04	382.3
12	1.6e-03	166.7
13	1.6e-03	166.7
14	7.7e-04	337.6
15	1.3e-03	206.3
16	1.3e-03	200.0
17	7.3e-04	356.1
18	7.3e-04	356.1
19	7.5e-04	346.6
20	7.4e-04	351.3
21	1.3e-03	203.1
22	1.3e-03	203.1
23	7.4e-04	351.3
24	704e-04	351.3
25	1.3e-03	201.5
26	1.3e-03	201.5
27	1.3e-03	203.1
28	1.3e-03	204.7
29	1.3e-03	204.7
30	1.3e-03	204.7
31	1.3e-03	203.1
32	7.5e-04	346.6
33	7.3e-04	356.1
34	1.3e-03	203.3
35	8.6e-04	302.3
36	2.5e-04	104.0
37	1.4e-3	192.5
38	8.3e-4	313.2
39	1.5e-03	178.2
40	8.0e-04	325
41	1.5e-03	178.2
42	7.6e-04	342.0

43	7.4e-04	351.3
44	7.4e-04	351.3
45	7.2e-04	361.1
46	1.3e-03	203.1
47	1.3e-03	204.7
48	8.3e-4	313.2
49	6.8e-04	382.3
50	1.5e-03	178.2
	Mean value= 2.50E-03 sec	**Mean value = 253.68 m/s**

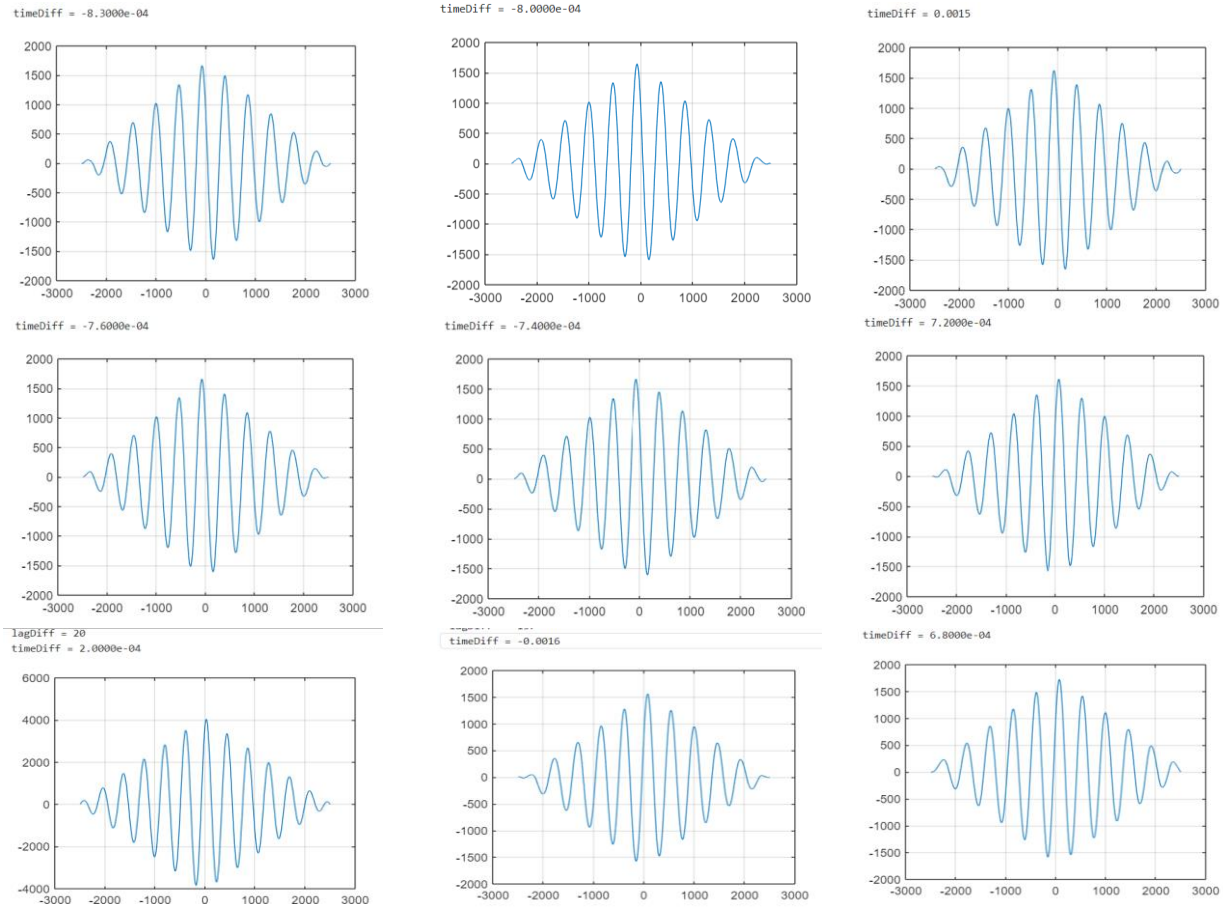

timeDiff = 0.0013

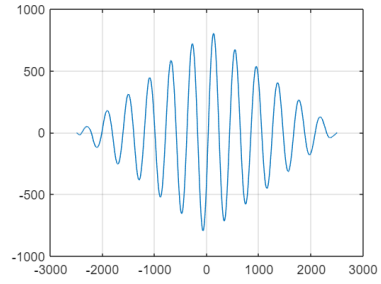

timeDiff = 7.7000e-04

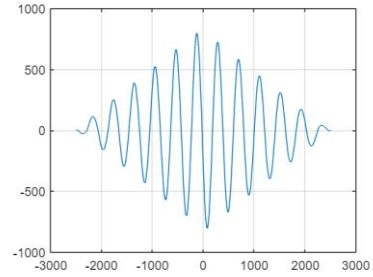

lagDiff = 126
timeDiff = 0.0013

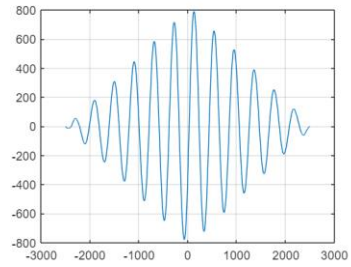

lagDiff = 130
timeDiff = 0.0013

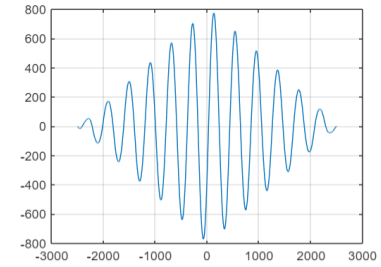

lagDiff = 73
timeDiff = 7.3000e-04

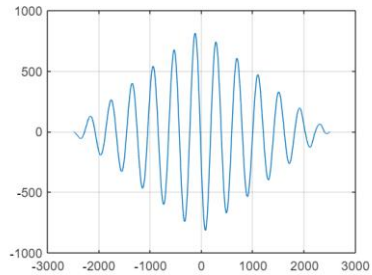

lagDiff = 73
timeDiff = 7.3000e-04

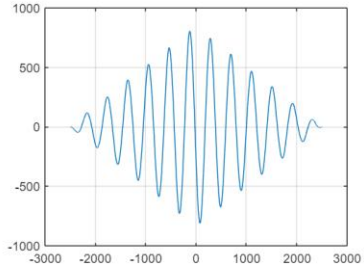

timeDiff = 7.5000e-04

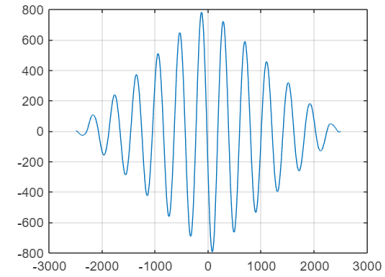

timeDiff = 7.4000e-04

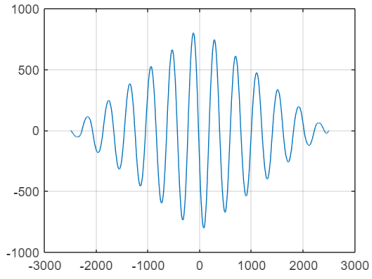

timeDiff = -0.0013

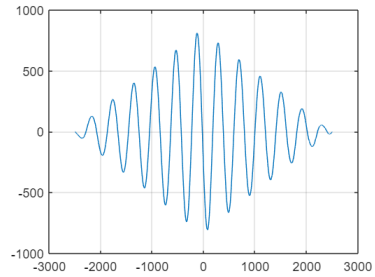

timeDiff = 0.0013

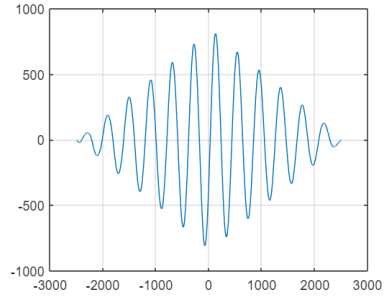

timeDiff = 7.4000e-04

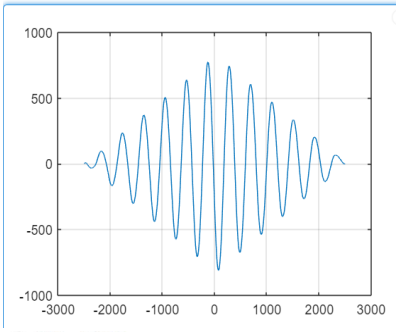

timeDiff = 7.4000e-04

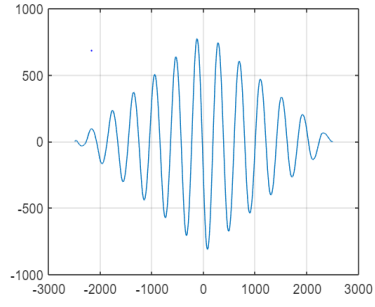

timeDiff = -0.0013

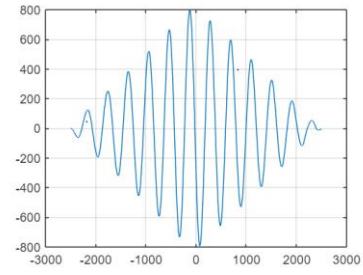

timeDiff = 0.0013

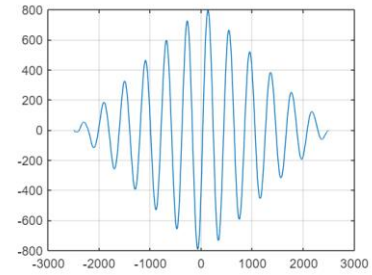

timeDiff = -0.0013

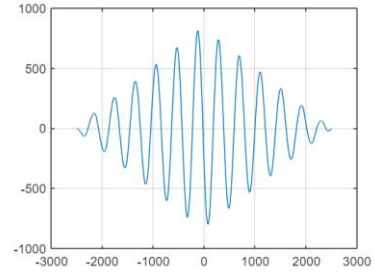

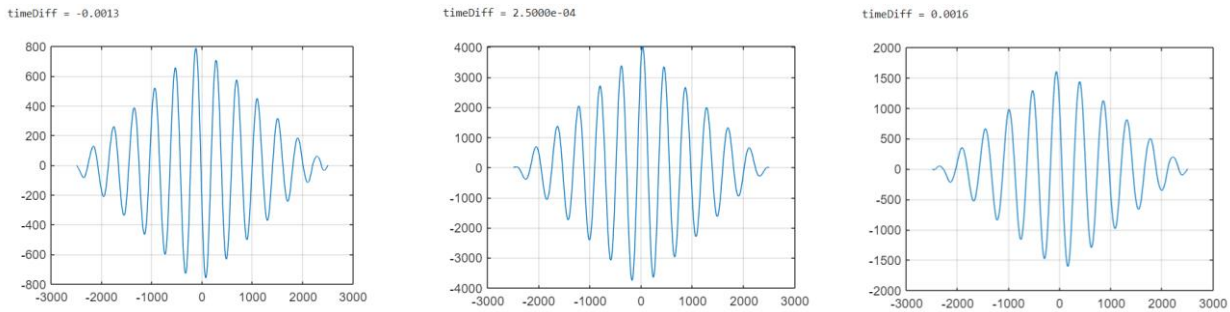

Figure A.2.3: Matlab result for Steel plate with defect using TOF

B. Appendix B

Table B.1: Frequency result calculated using FFT for Steel ring

Sr. No.	The frequency at mode 6 with a 4mm defect	The frequency at mode 6 with no defect	Difference
1	5834.3	5873.7	39.4
2	5834.3	5873.4	39.1
3	5834.3	5873.5	39.2
4	5834.4	5874.3	39.2
5	5834.4	5873.6	39.9
6	5834.3	5873.6	39.2
7	5831.4	5873.7	39.3
8	5834.5	5873.6	42.3
9	5834.3	5874.2	39.1
10	5834.2	5873.5	39.9
11	5834.5	5873.7	39.3
12	5834.2	5874.1	392
13	5834.1	5873.4	39.9
14	5834.3	5874.1	39.8
15	5833.3	5873.3	40
16	5834.3	5873.6	39.3
17	5832.1	5873.1	41
18	5833.8	5892.3	58.5

19	5834.1	5873.6	39.5
20	5834.4	5873.5	39.1
21	5834.2	5874.5	40.3
22	5833.6	5873.7	40.1
23	5834.1	5873.8	39.7
24	5833.4	5873.4	40
25	5834.1	5874.1	40
26	5833.7	5873.6	39.9
27	5833.6	5873.6	40
28	5834.1	5873.8	39.7
29	5833.8	5873.6	39.8
30	5834.4	5874.1	39.7
31	5834.4	5874.1	39.7
32	5834.2	5874.2	40
33	5834.5	5873.5	39
34	5834.1	5874.2	40.1
35	5834.6	5873.6	39
36	5834.3	5873.7	39.4
37	5834.5	5873.6	39.1
38	5834.3	5873.6	39.3
39	5832.3	5874.1	41.8
40	5832.1	5873.1	41
41	5834.2	5873.2	39
42	5832.4	5873.1	40.7
43	5834.5	5874.3	39.8
44	5832.1	5873.5	41.4
45	5833.6	5874.1	40.5
46	5834.2	5873.6	39.4
47	5834.1	5874.6	40.5
48	5833.6	5874.3	40.7
49	5834.2	5873.6	39.4
50	5833.8	5874.1	40.3
51	5832.1	5873.1	41
52	5833.8	5892.3	58.5
53	5834.6	5873.6	39
54	5834.3	5873.7	39.4
55	5832.1	5873.5	41.4
56	5833.6	5874.1	40.5
57	5834.1	5874.1	40
58	5833.7	5873.6	39.9
59	5834.1	5874.2	40.1
60	5834.6	5873.6	39
61	5834.3	5873.7	39.4
62	5834.5	5873.6	42.3
63	5834.3	5874.2	39.1
64	5834.2	5873.5	39.9

65	5832.1	5873.1	41
66	5834.3	5873.5	39.2
67	5834.4	5874.3	39.2
68	5834.4	5873.6	39.9
69	5834.3	5873.6	39.2
70	5831.4	5873.7	39.3
71	5834.5	5873.6	42.3
72	5834.3	5874.2	39.1
73	5834.2	5873.5	39.9
74	5834.5	5873.7	39.3
75	5834.2	5874.1	392
76	5834.1	5873.4	39.9
77	5834.3	5874.1	39.8
78	5833.3	5873.3	40
79	5834.3	5873.6	39.3
80	5832.1	5873.1	41
81	5833.8	5892.3	58.5
82	5834.1	5873.6	39.5
83	5834.4	5873.5	39.1
84	5834.2	5874.5	40.3
85	5833.6	5873.7	40.1
86	5834.1	5873.8	39.7
87	5833.4	5873.4	40
88	5834.1	5874.1	40
89	5833.7	5873.6	39.9
90	5833.6	5873.6	40
91	5834.1	5873.8	39.7
92	5833.8	5873.6	39.8
93	5834.4	5874.1	39.7
94	5834.4	5874.1	39.7
95	5834.2	5874.2	40
96	5834.5	5873.5	39
97	5834.1	5874.2	40.1
98	5834.6	5873.6	39
99	5834.3	5873.7	39.4
100	5834.5	5873.6	39.1
101	5834.3	5873.6	39.3
102	5832.3	5874.1	41.8
	Mean Value: 5833.88	**Mean value: 5874.27**	**Difference = 40**

The result shows the difference between the two frequency is between 38-42 Hz.

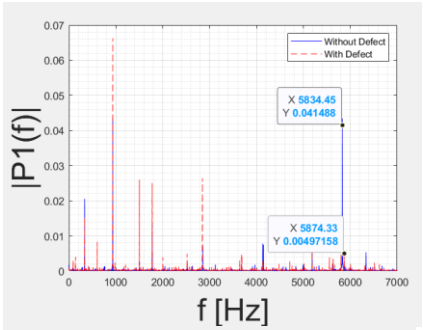
Without Defect
With Defect
X 5834.45
Y 0.041488
X 5874.33
Y 0.00497158
|P1(f)|
f [Hz]

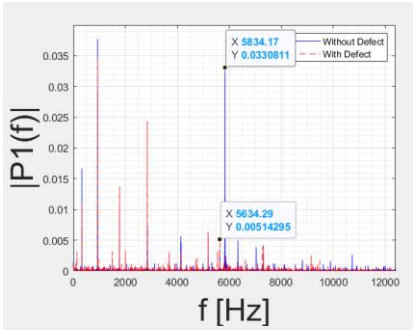
Without Defect
With Defect
X 5834.17
Y 0.0330811
X 5634.29
Y 0.00514295
|P1(f)|
f [Hz]

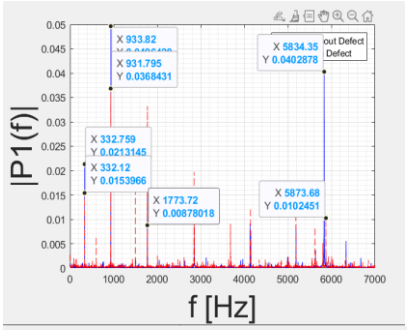
X 933.82
X 931.795
Y 0.0368431
X 5834.35
Y 0.0402878
X 332.759
Y 0.0213145
X 332.12
Y 0.0153966
X 1773.72
Y 0.00878018
X 5873.68
Y 0.0102451
|P1(f)|
f [Hz]

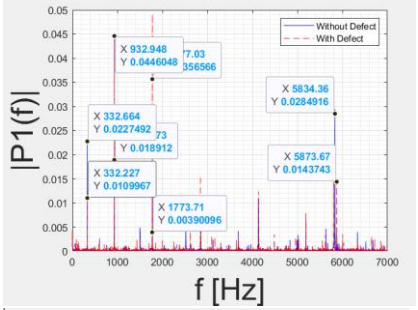
Without Defect
With Defect
X 932.948
Y 0.0446048
X 5834.36
Y 0.0284916
X 332.664
Y 0.0227492
X 332.227
Y 0.0109967
X 1773.71
Y 0.00390096
X 5873.67
Y 0.0143743
|P1(f)|
f [Hz]

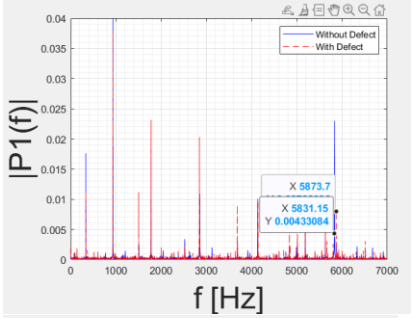
Without Defect
With Defect
X 5873.7
X 5831.15
Y 0.00433084
|P1(f)|
f [Hz]

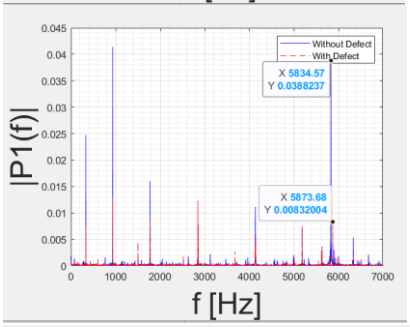
Without Defect
With Defect
X 5834.57
Y 0.0388237
X 5873.68
Y 0.00832004
|P1(f)|
f [Hz]

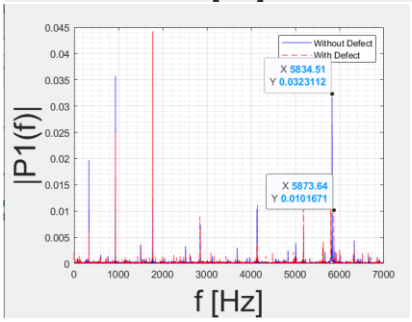
Without Defect
With Defect
X 5834.51
Y 0.0323112
X 5873.64
Y 0.0101671
|P1(f)|
f [Hz]

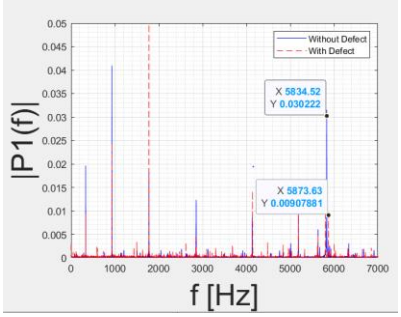
Without Defect
With Defect
X 5834.52
Y 0.030222
X 5873.63
Y 0.00907881
|P1(f)|
f [Hz]

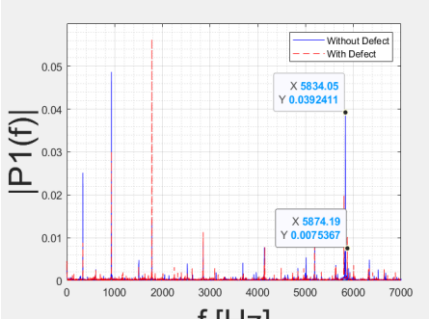
Without Defect
With Defect
X 5834.05
Y 0.0392411
X 5874.19
Y 0.0075367
|P1(f)|

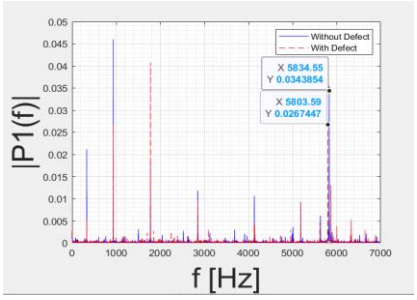
Without Defect
With Defect
X 5834.55
Y 0.0343854
X 5803.59
Y 0.0267447
|P1(f)|
f [Hz]

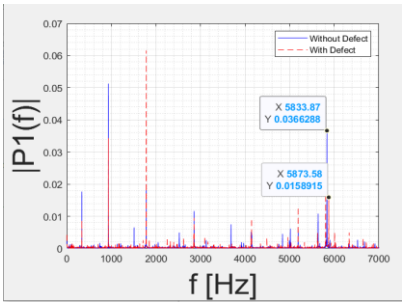
Without Defect
With Defect
X 5833.87
Y 0.0366288
X 5873.58
Y 0.0158915
|P1(f)|
f [Hz]

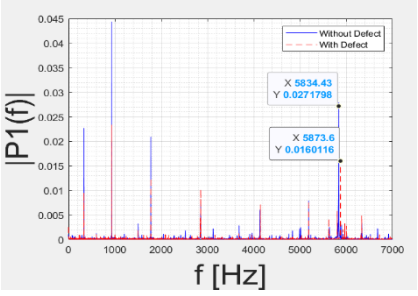
Without Defect
With Defect
X 5834.43
Y 0.0271798
X 5873.6
Y 0.0160116
|P1(f)|
f [Hz]

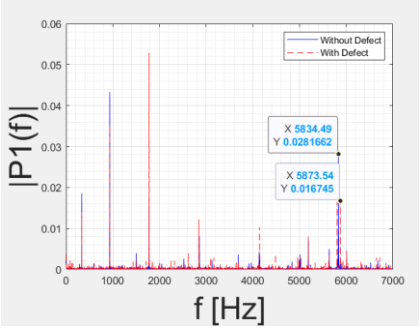
Without Defect
With Defect
X 5834.49
Y 0.0281662
X 5873.54
Y 0.016745
|P1(f)|
f [Hz]

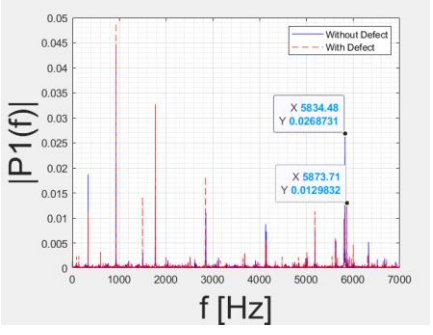
Without Defect
With Defect
X 5834.48
Y 0.0268731
X 5873.71
Y 0.0129832
|P1(f)|
f [Hz]

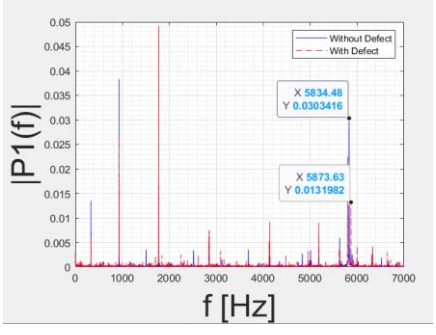
Without Defect
With Defect
X 5834.48
Y 0.0303416
X 5873.63
Y 0.0131982
|P1(f)|
f [Hz]

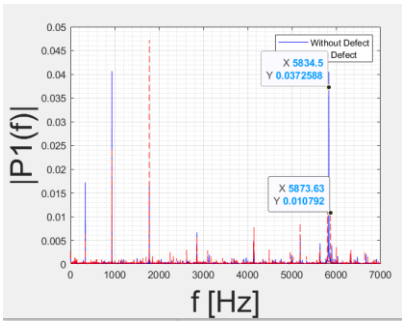
Without Defect
Defect
X 5834.5
Y 0.0372588
X 5873.63
Y 0.010792
|P1(f)|
f [Hz]

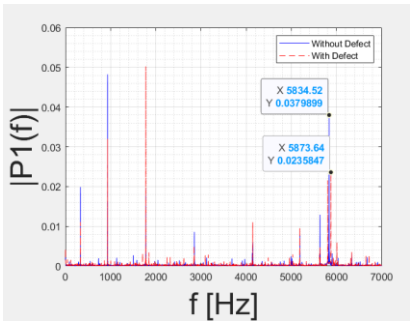
Without Defect
With Defect
X 5834.52
Y 0.0379899
X 5873.64
Y 0.0235847
|P1(f)|
f [Hz]

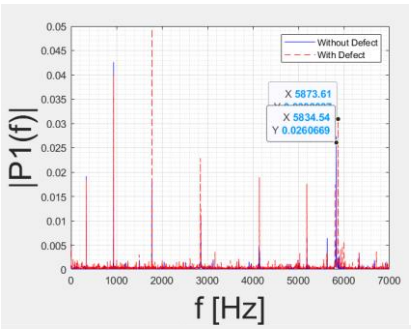
Without Defect
With Defect
X 5873.61
X 5834.54
Y 0.0260669
|P1(f)|
f [Hz]

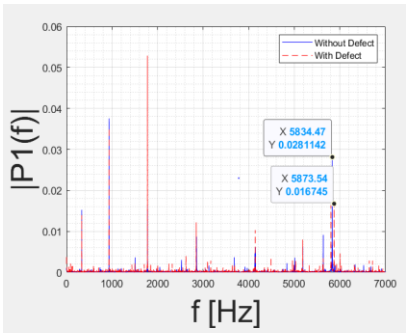
Without Defect
With Defect
X 5834.47
Y 0.0281142
X 5873.54
Y 0.016745
|P1(f)|
f [Hz]

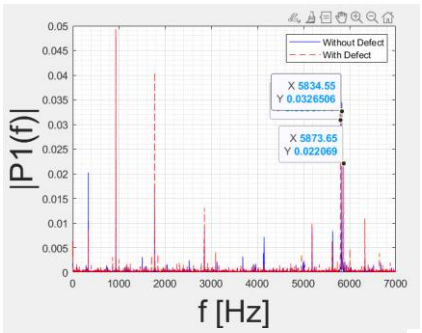
Without Defect
With Defect
X 5834.55
Y 0.0326506
X 5873.65
Y 0.022069
|P1(f)|
f [Hz]

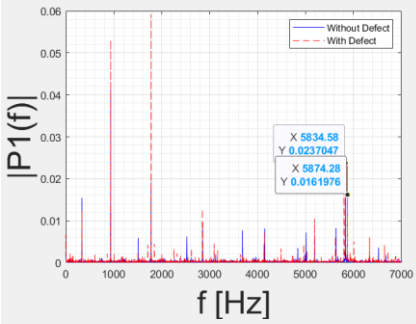
Without Defect
With Defect
X 5834.58
Y 0.0237047
X 5874.28
Y 0.0161976
|P1(f)|
f [Hz]

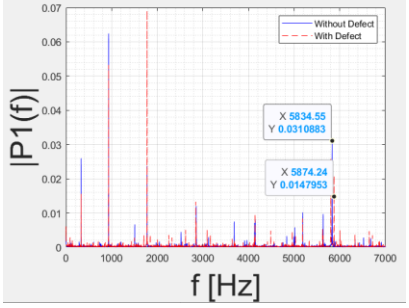
Without Defect
With Defect
X 5834.55
Y 0.0310883
X 5874.24
Y 0.0147953
|P1(f)|
f [Hz]

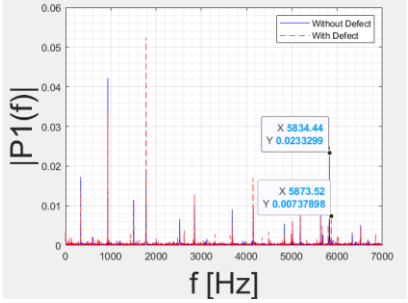
Without Defect
With Defect
X 5834.44
Y 0.0233299
X 5873.52
Y 0.00737898
|P1(f)|
f [Hz]

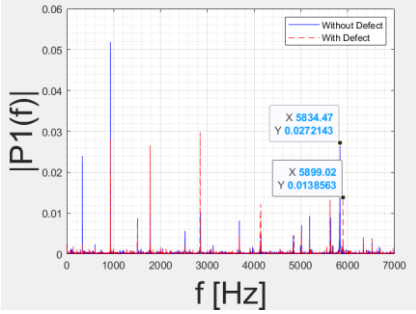
Without Defect
With Defect
X 5834.47
Y 0.0272143
X 5899.02
Y 0.0138563
|P1(f)|
f [Hz]

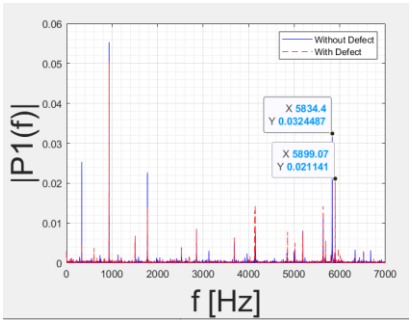
Without Defect
With Defect
X 5834.4
Y 0.0324487
X 5899.07
Y 0.021141
|P1(f)|
f [Hz]

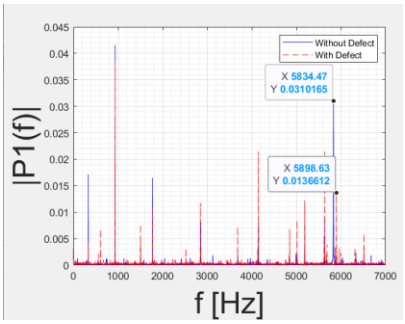
Without Defect
With Defect
X 5834.47
Y 0.0310165
X 5898.63
Y 0.0136612
|P1(f)|
f [Hz]

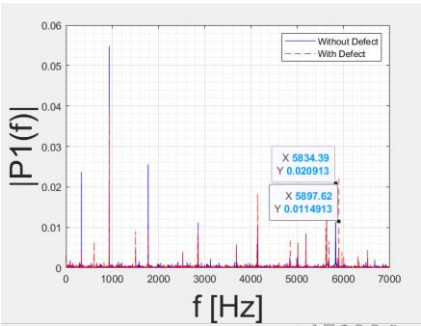
Without Defect
With Defect
X 5834.39
Y 0.020913
X 5897.62
Y 0.0114913
|P1(f)|
f [Hz]

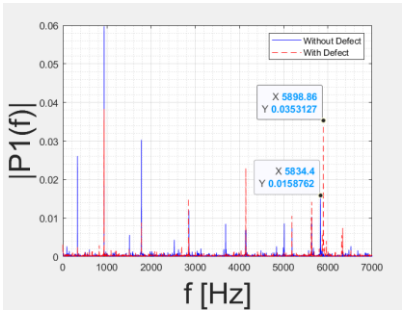
Without Defect
With Defect
X 5898.86
Y 0.0353127
X 5834.4
Y 0.0158762
|P1(f)|
f [Hz]

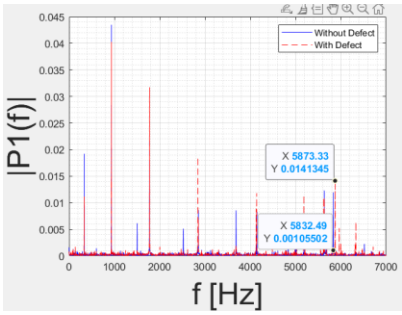
Without Defect
With Defect
X 5873.33
Y 0.0141345
X 5832.49
Y 0.00105502
|P1(f)|
f [Hz]

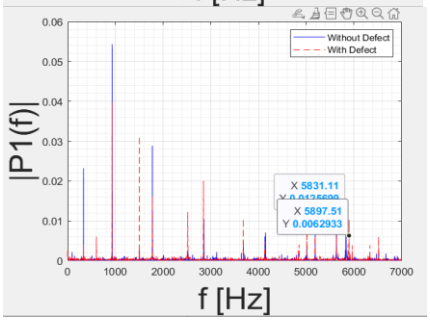
Without Defect
With Defect
X 5831.11
X 5897.51
Y 0.0062933
|P1(f)|
f [Hz]

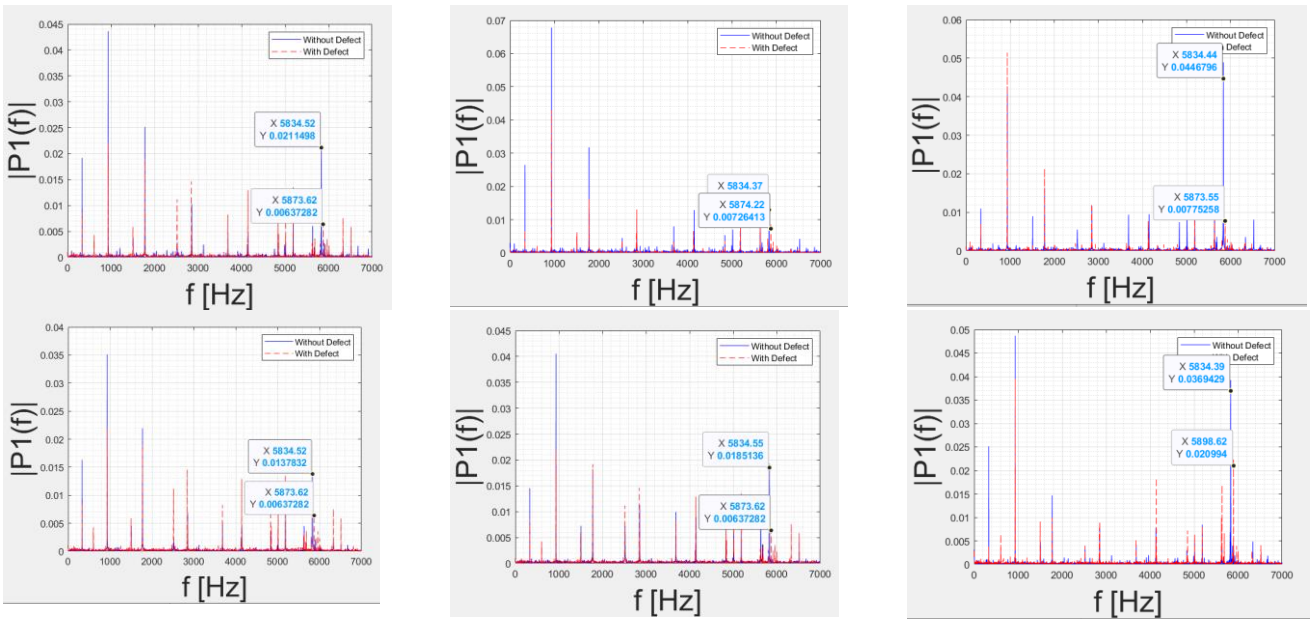

Figure B.1: Frequency Response

References

[1] Curtis, F. (2009). Peak globalization: Climate change, oil depletion and global trade. Ecological economics, 69(2), 427-434.

[2] Xu, Mengqiao, et al. (2020). Modular gateway-ness connectivity and structural core organization in maritime network science. Nature Communications 11(1), 2849.

[3] Ajit Nair, K. Sivaprasad & C.G. Nandakumar (2017) Crack assessment criteria for ship hull structure based on ship operational life, Cogent Engineering, 4:1, 1345044, DOI: 10.1080/23311916.2017.1345044

[4] Laura Poggi, Tomaso Gaggero, Marco Gaiotti, Enrico Ravina, Cesare Mario Rizzo, (2020). Recent developments in remote inspections of ship structures,International Journal of Naval Architecture and Ocean Engineering,Volume 12,Pages 881-891,ISSN 2092-6782, DOI: https://doi.org/10.1016/j.ijnaoe.2020.09.001.

[5] Vukelic, G.; Vizentin, G.; Brnic, J.; Brcic, M.; Sedmak, F. (2021). Long-Term Marine Environment Exposure Effect on Butt-Welded Shipbuilding Steel. *J.Mar.Sci.Eng.*, *9*,491,https://doi.org/10.3390/jmse9050491.

[6] Eich, M., Bonnin-Pascual, F., Garcia-Fidalgo, E., Ortiz, A., Bruzzone, G., Koveos, Y., & Kirchner, F. (2014). A robot application for marine vessel inspection. *Journal of Field Robotics*, *31*(2), 319-341. **https://doi.org/10.1002/rob.21498**

[7] Laura Poggi, Tomaso Gaggero, Marco Gaiotti, Enrico Ravina, Cesare Mario Rizzo,Recent developments in remote inspections of ship structures, International Journal of Naval Architecture and Ocean Engineering, Volume 12,2020,Pages 881-891,ISSN 2092-6782, https://doi.org/10.1016/j.ijnaoe.2020.09.001

[8] Bonnin-Pascual, F., & Ortiz, A. (2019). On the use of robots and vision technologies for the inspection of vessels: A survey on recent advances. *Ocean Engineering*, *190*, 106420. DOI: https://doi.org/10.1016/j.oceaneng.2019.106420

[9] Unyime O Akpan, T.S Koko, B Ayyub, T.E. (2002), Dunbar,Risk assessment of aging ship hull structures in the presence of corrosion and fatigue,Marine Structures,Volume 15, Issue 3 ,Pages 211-231,ISSN 0951-8339,https://do.org/10.1016/S0951-8339(01)00030-2.

[10] Animah, I.; Shafiee, M. (2018). Condition assessment, remaining useful life prediction and life extension decision making for offshore oil and gas assets. J. Loss Prev. Process Ind., 53, 17–28. DOI:10.1016/j.jlp.2017.04.030

[11] Abbas, M., & Shafiee, M. (2018). Structural Health Monitoring (SHM) and Determination of Surface Defects in Large Metallic Structures using Ultrasonic Guided Waves. *Sensors (Basel, Switzerland)*, *18*(11), 3958. https://doi.org/10.3390/s18113958

[12] Singh, R. (2014). Corrosion Principles and Types of Corrosion. In R. Singh (Ed.), Corrosion Control for Offshore Structures (pp. 7-40). Gulf Professional Publishing. ISBN 9780124046153. https://doi.org/10.1016/B978-0-12-404615-3.00002-4

[13] Zhang, X., Wang, S., Wang, X., Cui, Z., Cui, H., & Li, Y. (2023). The stress corrosion cracking behavior of N80 carbon steel under a crevice in an acidic solution containing different concentrations of NaCl. Corrosion Science, 216, 111068. https://doi.org/10.1016/j.corsci.2023.111068.

[14] Obeyesekere, N. U. (2017). Pitting Corrosion. In A. M. El-Sherik (Ed.), Trends in Oil and Gas Corrosion Research and Technologies (pp. 215-248). Woodhead Publishing Series in Energy. Woodhead Publishing. ISBN 9780081011058. https://doi.org/10.1016/B978-0-08-101105-8.00009-7.

[15] Zheng, R., Zhao, X., Dong, L., Liu, G., Huang, Y., & Xu, Y. (2022). On the cavitation erosion-corrosion of pipeline steel at different locations of Venturi pipe. Engineering Failure Analysis, 138, 106333. https://doi.org/10.1016/j.engfailanal.2022.106333

[16] Wan, H., Zhang, T., Wang, J., Rao, Z., Zhang, Y., Li, G., Gu, T., & Liu, H. (2023). Effect of alloying element content on anaerobic microbiologically influenced corrosion sensitivity of stainless steels in enriched artificial seawater. Bioelectrochemistry, 150, 108367. https://doi.org/10.1016/j.bioelechem.2023.108367

[17] Prabhuraj, P., Rajakumar, S., Sonar, T., Ivanov, M., Rajkumar, I., & Raja, D. E. (2022). Effect of retrogression and reaging (RRA) on pitting and stress corrosion cracking (SCC) resistance of stir zone of high strength AA7075-T651 alloy joined by friction stir welding. International Journal of Lightweight Materials and Manufacture. Advance online publication. https://doi.org/10.1016/j.ijlmm.2022.12.002

[18] Shabani Mahalli, M., Ahmadi, A., & Sabouri, M. (2022). Investigation of intergranular stress corrosion cracking in a failed 347H stainless steel furnace tube. Engineering Failure Analysis, 142, 106835. https://doi.org/10.1016/j.engfailanal.2022.106835

[19] Li, Q., Yao, Q., Sun, L., Ma, H., Zhang, C., & Wang, N. (2023). Effect of micro-galvanic corrosion on corrosion fatigue cracking of the weld joint of high strength bridge steel. International Journal of Fatigue, 170, 107568. https://doi.org/10.1016/j.ijfatigue.2023.107568.

[20] Zan, Y., Guo, R., Yuan, L., Ma, Q., Zhou, A., & Wu, Z. (2021). Experimental study of a suspended subsea module at different positions in the splash zone. Marine Structures, 77, 102935. https://doi.org/10.1016/j.marstruc.2021.102935

[21] Wang, H. H., & Du, M. (2017). Corrosion behavior of a low-carbon steel in simulated marine splash zone. *Acta Metallurgica Sinica (English Letters)*, *30*, 585-593.Anderson, M. R. (1987). Non-destructive testing of offshore structures. *NDT international*, *20*(1), 17-21. DOI: https://doi.org/10.1007/s40195-017-0535-1

[22] Giurgiutiu, V. (2014). Chapter 1 - Introduction. In V. Giurgiutiu (Ed.), Structural Health Monitoring with Piezoelectric Wafer Active Sensors (Second Edition) (pp. 1–19). Oxford: Academic Press. https://doi.org/10.1016/B978-0-12-418691-0.00001-0

[23] Giurgiutiu, V. (2016). Chapter 8 - Other Sensors for SHM of Aerospace Composites. In V. Giurgiutiu (Ed.), Structural Health Monitoring of Aerospace Composites (pp. 297–315). Oxford: Academic Press. https://doi.org/10.1016/B978-0-12-409605-9.00008-8

[24] Lehmann, M., Büter, A., Frankenstein, B., Schubert, F., & Brunner, B. (2006, September). Monitoring System for Delamination Detection - Qualification of Structural Health Monitoring (SHM) Systems.

[25] Kralovec, C., & Schagerl, M. (2020). Review of Structural Health Monitoring Methods Regarding a Multi-Sensor Approach for Damage Assessment of Metal and Composite Structures. Sensors, 20(3), 826. https://doi.org/10.3390/s20030826

[26] Deepak, J. R., Raja, V. B., Srikanth, D., Surendran, H., & Nickolas, M. M. (2021). Non-destructive testing (NDT) techniques for low carbon steel welded joints: A review and experimental study. Materials Today: Proceedings, 44, 3732-3737.

[27] J.R. Deepak, V.K. Bupesh Raja, D. Srikanth, H. Surendran, & M.M. Nickolas. (2021). Non-destructive testing (NDT) techniques for low carbon steel welded joints: A review and experimental study. Materials Today: Proceedings, 44(5), 3732-3737. https://doi.org/10.1016/j.matpr.2020.11.578

[28] Wan Abdullah Zawawi, N.A., Liew, M.S., Alaloul, W., Shawn, L., Imran, M., & Toloue, I. (2019). Non-Destructive Testing Techniques for Offshore Underwater Decommissioning Projects through Cutting Detection: A State of Review. Society of Petroleum Engineers. https://doi.org/10.2118/199191-MS

[29] Demsetz, L., & Cabrera, J. (1999). Detection probability assessment of visual inspection of ships (Ship Structure Committee Report No. SSC-408). Washington, DC: Ship Structure Committee. DOI- N/A

[30] Zhang, J., Cho, Y., Kim, J., Malikov, A. K. U., Kim, Y. H., Yi, J. H., & Li, W. (2021). Non-destructive evaluation of coating thickness using water immersion ultrasonic testing. Coatings, 11(11), 1421. https://doi.org/10.3390/coatings11111421

[31] Ditchburn, R. J., Burke, S. K., & Scala, C. M. (1996). NDT of welds: State of the art. NDT & E International, 29(2), 111-117. https://doi.org/10.1016/0963-8695(96)00010-2.

[32] Sakai, K., Morita, K., Haga, Y., Kiwa, T., Inoue, K., & Tsukada, K. (2015). Automatic scanning system for back-side defect of steel structure using magnetic flux leakage method. IEEE Transactions on Magnetics, 51(11), 1-3, Art no. 6202103. https://doi.org/10.1109/TMAG.2015.2453211.

[33] Blitz, J. (1987). Eddy current testing of metals. Materials & Design, 8(6), 340-345. https://doi.org/10.1016/0261-3069(87)90084-7.

[34] Swiderski, W. (2016). Detecting defects in marine structures by using eddy current infrared thermography. Applied Optics, 55(34), D17-D21. https://doi.org/10.1364/AO.55.000D17.

[35] Zhong, S. (2019). Progress in terahertz nondestructive testing: A review. Frontiers of Mechanical Engineering, 14(3), 273-281. https://doi.org/10.1007/s11465-018-0495-9

[36] Battley, M., Skeates, A., & Holmqvist, A. (2002). Non-destructive inspection of marine composite structures. In Proceedings of the High Performance Yacht Design Conference.

[37] Wang, G., Lee, M., Serratella, C., Botten, S., Ternowchek, S., Ozevin, D., ... & Scott, R. (2010). Testing of acoustic emission technology to detect cracks and corrosion in the marine environment. Journal of Ship Production and Design, 26(2), 106-110. https://doi.org/10.1177/875647391002600206

[38] Maldague, X. (2001). Theory and practice of infrared technology for nondestructive testing.

[39] Rayleigh, L. (1885). On waves propagated along the plane surface of an elastic solid. Proceedings of the London Mathematical Society, s1-17(1), 4-11. doi: 10.1112/plms/s1-17.1.4

[40] Silva, C., Rocha, B., & Suleman, A. (2010). Guided Lamb waves based structural health monitoring through a PZT network system. doi: 10.4028/www.scientific.net/AMR.93-94.367

[41] C. Covaci and A. Gontean, “Piezoelectric Energy Harvesting Solutions: A Review,” Sensors, vol. 20, no. 12, Art. no. 12, Jan. 2020, doi: 10.3390/s20123512

[42] Giurgiutiu, V., & Cuc, A. (2005). Embedded non-destructive evaluation for structural health monitoring, damage detection, and failure prevention. Shock and Vibration Digest, 37(2), 83. https://doi.org/10.1177/0583102405052812

[43] Demma, A.; Cawley, P.; Lowe, M. Scattering of the fundamental shear horizontal mode from steps and notches in plates. J. Acoust. Soc. Am. 2003, 113, 1880–1891.

[44] Pau, A.; Achillopoulou, D.V. Interaction of Shear and Rayleigh-Lamb Waves with Notches and Voids in Plate Waveguides. Materials 2017, 10, 841.

[45] Keilers Jr, C. H., & Chang, F. K. (1995). Identifying delamination in composite beams using built-in piezoelectrics: part I—experiments and analysis. Journal of Intelligent Material Systems and Structures, 6(5), 649-663. https://doi.org/10.1177/1045389X9500600510

[46] Masserey, B., & Fromme, P. (2009). Surface defect detection in stiffened plate structures using Rayleigh-like waves. Ndt & E International, 42(6), 564-572.

[47] Salinas, N., & Rose, J. L. (2007). Guided wave structural health monitoring of pipelines: A review of the technology and case studies. Structural Health Monitoring, 6(2), 161–173. https://doi.org/10.1177/1475921707078456

[48] Gao, H., & Rose, J. L. (2005). Guided waves in damage detection and evaluation of aerospace structures: A review. Shock and Vibration Digest, 37(2), 93–105. https://doi.org/10.1177/0583102405053781

[49] Park, S., Yun, C. B., Roh, Y., & Lee, J. J. (2006). PZT-based active damage detection techniques for steel bridge components. Smart Materials and Structures, 15(4), 957.

[50] Michaels, J. E., & Michaels, T. E. (2003). Guided wave techniques for pipeline inspection. In S. S. Udpa & J. J. Lesko (Eds.), Review of Progress in Quantitative Nondestructive Evaluation (Vol. 22A, pp. 962–968). Springer. https://doi.org/10.1007/978-1-4757-3794-7_128

[51] Schmerr, L. W. (2016). Fundamentals of ultrasonic nondestructive evaluation (Vol. 122, pp. 85-140). New York, NY, USA:: Springer.

[52] Shahzad, K., Ahmad, A. M. S., & Khan, M. A. (n.d.). Ultrasonic testing using time of flight diffraction technique (TOFD). Retrieved March 5, 2023, from https://www.osti.gov/etdeweb/biblio/21498501

[53] Mitra, M., & Gopalakrishnan, S. (2016). Guided wave based structural health monitoring: A review. Smart Materials and Structures, 25(5), 053001. https://doi.org/10.1088/0964-1726/25/5/053001

[54] Toa, M., & Whitehead, A. (2020). Ultrasonic sensing Basics. Dallas: Texas Instruments.

[55] Feeney, A., Kang, L., & Dixon, S. (2018). High-frequency measurement of ultrasound using flexural ultrasonic transducers. IEEE Sensors Journal, 18(13), 5238-5244. doi: 10.1109/JSEN.2018.2826509

[56] Olisa, S. C., Khan, M. A., & Starr, A. (2021). Review of current guided wave ultrasonic testing (GWUT) limitations and future directions. Sensors, 21(3), 811. doi: 10.3390/s21030811

[57] Gorgin, R., Luo, Y., & Wu, Z. (2020). Environmental and operational conditions effects on Lamb wave based structural health monitoring systems: A review. Ultrasonics, 105, 106114. https://doi.org/10.1016/j.ultras.2020.106114

[58] Quek, S. T., Tua, P. S., & Jin, J. (2007). Comparison of plain piezoceramics and inter-digital transducer for crack detection in plates. Journal of Intelligent Material Systems and Structures, 18(9), 949-961.

[59] Raghavan, A. (2007). Guided-wave structural health monitoring (Doctoral dissertation). Retrieved from ProQuest Dissertations and Theses database. (UMI No. 3265896)

[60] Bonnin-Pascual, F., & Ortiz, A. (2018). A novel approach for defect detection on vessel structures using saliency-related features. Ocean Engineering, 149, 397-408. https://doi.org/10.1016/j.oceaneng.2017.12.027

[61] Lynn, D.C., & Bohlander, G.S. (1999). Performing ship hull inspections using a remotely operated vehicle. In IEEE/MTS OCEANS Conference (Vol. 2, pp. 555-562).

[62] Newsome, S.M., & Rodocker, J. (2009). Effective technology for underwater hull and infrastructure inspection. In IEEE/MTS OCEANS Conference (pp. 1-6).

[63] Ishizu, K., Sakagami, N., Ishimaru, K., Shibata, M., Onishi, H., Murakami, S., & Kawamura, S. (2012). Ship hull inspection using a small underwater robot with a mechanical contact mechanism. Journal of Field Robotics, 29(6), 1011-1021

[64] Ishizu, K., Sakagami, N., Ishimaru, K., Shibata, M., Onishi, H., Murakami, S., & Kawamura, S. (2012, May). Ship hull inspection using a small underwater robot with a mechanical contact mechanism. In 2012 Oceans-Yeosu (pp. 1-6). IEEE

[65] Younkyu, K., Joonhong, K., Jungbin, K., Kima, D., & Minsu, P. Development of Advanced Underwater Robot and Inspection System for Nuclear Reactor.

[66] Narewski, M. (2009). HISMAR-underwater hull inspection and cleaning system as a tool for ship propulsion system performance increase. Journal of Polish CIMAC, 4(2), 227-232.

[67] Bonnin-Pascual, F., & Ortiz, A. (2019). On the use of robots and vision technologies for the inspection of vessels: A survey on recent advances. Ocean Engineering, 190, 106420.

[68] Sahoo, A., Dwivedy, S. K., & Robi, P. S. (2019). Advancements in the field of autonomous underwater vehicle. Ocean Engineering, 181, 145-160. https://doi.org/10.1016/j.oceaneng.2019.04.011

[69] Narewski, M. (2009). HISMAR-underwater hull inspection and cleaning system as a tool for ship propulsion system performance increase. Journal of Polish CIMAC, 4(2), 227-232.

[70] Wei, J., Li, X., & Yu, Y. (2021). Research on the Path Planning and Obstacle Avoidance Algorithm of Autonomous Underwater Vehicle Based on Improved Particle Swarm Optimization. IEEE Access, 9, 66769-66778. doi: 10.1109/access.2021.3081933

[71] Shrestha, P. (2019). Underwater Wireless Optical Communication Channel: Analysis and Improvement Using Low-Density Parity-Check Codes. IEEE Access, 7, 44152-44159. doi: 10.1109/access.2019.2903812

[72] Hu, K., Weng, C., Zhang, Y., Jin, J., & Xia, Q. (2022). An overview of underwater vision enhancement: from traditional methods to recent deep learning. Journal of Marine Science and Engineering, 10(2), 241.

[73] Jaffe, J. S., & McGlamery, B. L. (1971). Improved In-water visibility by horizontally polarized light. Applied Optics, 10(12), 2669-2676. doi: 10.1364/ao.10.002669

[74] Chen, Y., Huang, C., Cao, X., & Li, L. (2020). Underwater object recognition based on the feature fusion of RGB and texture images. IEEE Access, 8, 52358-52370. doi: 10.1109/access.2020.2989674

[75] M. Eich and T. Vögele, "Design and control of a lightweight magnetic climbing robot for vessel inspection," 2011 19th Mediterranean Conference on Control & Automation (MED), Corfu, Greece, 2011, pp. 1200-1205, doi: 10.1109/MED.2011.5983075.

[76] Gupta, S. G., Ghonge, M., & Jawandhiya, P. M. (2013). Review of unmanned aircraft system (UAS). International Journal of Advanced Research in Computer Engineering & Technology (IJARCET), 2(4). Retrieved from https://ssrn.com/abstract=3451039 or http://dx.doi.org/10.2139/ssrn.3451039

[77] Nooralishahi, P., Ibarra-Castanedo, C., Deane, S., López, F., Pant, S., Genest, M., Avdelidis, N. P., & Maldague, X. P. V. (2021). Drone-Based Non-Destructive Inspection of Industrial Sites: A Review and Case Studies. Drones, 5(4), 106. https://doi.org/10.3390/drones5040106

[78] Kim, M.-k., Wang, Q., & Li, H. (2019). Non-contact sensing based geometric quality assessment of buildings and civil structures: A review. Automation in Construction, 100, 163-179. doi:10.1016/j.autcon.2019.01.002

[79] Arafat, M. Y., Alam, M. M., & Moh, S. (2023). Vision-Based Navigation Techniques for Unmanned Aerial Vehicles: Review and Challenges. Drones, 7(2), 89. https://doi.org/10.3390/drones7020089

[80] McAree, O., Aitken, J. M., & Veres, S. M. (2016, August). A model based design framework for safety verification of a semi-autonomous inspection drone. In 2016 UKACC 11th International conference on control (CONTROL) (pp. 1-6). IEEE.

[81] Wu, Y., Qin, Y., Wang, Z., & Jia, L. (2018). A UAV-based visual inspection method for rail surface defects. Applied Sciences, 8(7), 1028. https://doi.org/10.3390/app8071028

[82] Sabato, A., Niezrecki, C., Dabetwar, S., Kulkarni, N. N., Bottalico, F., & Nieduzak, T. (2022). Advancements in structural health monitoring using combined computer-vision and unmanned aerial vehicles approaches. Lecture Notes in Civil Engineering, 254. https://doi.org/10.1007/978-981-17-4064-8_12

[83] Blaney, S., & Gupta, R. (2018). Unmanned aerial vehicle-based sounding of subsurface concrete defects. Journal of the Acoustical Society of America, 144(4), 2269–2269. https://doi.org/10.1121/1.5054012

[84] Adams, R. D. and Cawley, P. Vibration techniques in nondestructive testing. Research techniques in NDT, 1985, 8 (Ed: R. S.Sharpe) (in press).

[85] Nagy, K., Dousis, D. A., & Finch, R. D. (1978). Detection of flaws in railroad wheels using acoustic signatures. Journal of Engineering for Industry, 100(4), 459-465. https://doi.org/10.1115/1.3439461

[86] Kiefel, D., Stoessel, R., & Grosse, C. (2015). Quantitative impact characterization of aeronautical CFRP materials with non-destructive testing methods. DOE Office of Scientific and Technical Information (OSTI.GOV). https://www.osti.gov/biblio/22391287-quantitative-impact-characterization-aeronautical-cfrp-materials-non-destructive-testing-methods

[87] Georgeson, G. E. (2004). Damage Detection Device and Method. The Boeing Company, Seattle, WA.

[88] Esola, S., Bartoli, I., Horner, S. E., Lanza di Scalea, F., & Meo, M. (2017). Defect detection via instrumented impact in thick-sectioned laminate composites. Journal of Nondestructive Evaluation, 36(3), 47. https://doi.org/10.1007/s10921-017-0422-8

[89] Cawley, P. (1985). Non-destructive testing of mass produced components by natural frequency measurements. Proceedings of the Institution of Mechanical Engineers, Part B: Journal of Engineering Manufacture, 199(3), 161-168.

[90] Kim, S. J. (2015). Damage detection in composite under in-plane load using tap test. Journal of Mechanical Science and Technology, 29(1), 199-207. doi:10.1007/s12206-014-1103-5

[91] Usamentiaga, R., Venegas, P., Guerediaga, J., Vega, L., Molleda, J., & Bulnes, F. G. (2014). Infrared thermography for temperature measurement and non-destructive testing. Sensors (Basel), 14(7), 12305–12348. https://doi.org/10.3390/s140712305

[92] Madruga, F. J., Sfarra, S., & Real, E. (2020). Complementary use of active infrared thermography and optical coherent tomography in non-destructive testing inspection of ancient marquetries. Journal of Nondestructive Evaluation, 39(2), 39. https://doi.org/10.1007/s10921-020-00683-4

[93] Ibarra-Castanedo, C., Tarpani, J. R., & Maldague, X. P. (2013). Nondestructive testing with thermography. European Journal of Physics, 34(6), S91.

[94] Wiecek, B. (2006, January). Review on thermal image processing for passive and active thermography. In 2005 IEEE Engineering in Medicine and Biology 27th Annual Conference (pp. 686-689). IEEE.

[95] Ibarra-Castanedo, C., Genest, M., Piau, J. M., Guibert, S., Bendada, A., & Maldague, X. P. (2007). Active infrared thermography techniques for the nondestructive testing of materials. In Ultrasonic and advanced methods for nondestructive testing and material characterization (pp. 325-348).

[96] Tran, Q. H., Han, D., Kang, C., Haldar, A., & Huh, J. (2017). Effects of ambient temperature and relative humidity on subsurface defect detection in concrete structures by active thermal imaging. Sensors, 17(8), 1718.

[97] Richards, W. L. (1986). Development of an electronic tap hammer for composite materials. Review of Progress in Quantitative Nondestructive Evaluation, 5, 1485-1492. https://doi.org/10.1007/978-1-4615-8180-9_205

[98] Lee, C., & Kim, K. (2013). Non-destructive evaluation of composite material using an instrumented impact hammer. Composites Part B: Engineering, 45(1), 1261-1266. https://doi.org/10.1016/j.compositesb.2012.07.034

[99] Marinetti, S., & Vavilov, V. (2010). IR thermographic detection and characterization of hidden corrosion in metals: General analysis. Corrosion science, 52(3), 865-872.

[100] Han, J. S., & Park, J. H. (2004). Detection of corrosion steel under an organic coating by infrared photography. Corrosion science, 46(4), 787-793.

[101] Jönsson, M., Rendahl, B., & Annergren, I. (2010). The use of infrared thermography in the corrosion science area. Materials and Corrosion, 61(11), 961-965.

[102] Schönberger, A., Virtanen, S., Giese, V., Schröttner, H., & Spießberger, C. (2012). Non-destructive detection of corrosion applied to steel and galvanized steel coated with organic paints by the pulsed phase thermography. *Materials and Corrosion*, *63*(3), 195-199.

[103] Liu, Z., Genest, M., & Krys, D. (2012). Processing thermography images for pitting corrosion quantification on small diameter ductile iron pipe. Ndt & E International, 47, 105-115.

[104] Vavilov, V. P., Grintsato, E., & Bizon, P. (1995). Detecting corrosion in steel products by dynamic infrared thermography. Russian Journal of Nondestructive Testing, 30(9).

[105] Hermanson, K. S., & Sandor, B. I. (1998). Corrosion fatigue modeling via differential infrared thermography. Experimental Techniques, 22, 19-21.

[106] Chung, L., Paik, I. K., Cho, S. H., & Roh, Y. S. (2006). Infrared thermographic technique to measure corrosion in reinforcing bar. In Key engineering materials (Vol. 321, pp. 821-824). Trans Tech Publications Ltd.

[107] Shen, G., & Li, T. (2007). Infrared thermography for high-temperature pressure pipe. Insight-Non-Destructive Testing and Condition Monitoring, 49(3), 151-153.

[108] Bison, P., Ceseri, M., & Inglese, G. (2010, March). Mapping corrosion of metallic slab by thermography. In Journal of Physics: Conference Series (Vol. 214, No. 1, p. 012073). IOP Publishing.

[109] Wang, Boyu, and Rishi Gupta. "Analyzing bond-deterioration during freeze-thaw exposure in cement-based repairs using non-destructive methods." Cement and Concrete Composites 115 (2021): 103830.

[110] Garbatov, Y., Guedes Soares, C., Ok, D., Pu, Y., Rizzo, C. M., Rizzuto, E., ... & Parmentier, G. (2006, January). Modelling strength degradation phenomena and inspections used for reliability assessment based on maintenance planning. In International Conference on Offshore Mechanics and Arctic Engineering (Vol. 47489, pp. 69-78).

[111] Viljoen, H. C., Mahomed, N., Cupido, L. H., & Mitchell, G. P. (2022). Effect of corrosion thinning on depth of operation: Case study of an HY-80 steel submarine pressure hull. Marine Structures, 81, 103103. https://doi.org/10.1016/j.marstruc.2021.103103

[112] Pau, A.; Achillopoulou, D.V. Interaction of Shear and Rayleigh-Lamb Waves with Notches and Voids in Plate Waveguides. Materials 2017, 10, 841.

[113] Wang, S.; Huang, S.; Zhao, W.; Wei, Z. 3D modeling of circumferential SH guided waves in pipeline for axial cracking detection in ILI tools. Ultrasonics 2015, 56, 325–331.

[114] Zhang, H.; Du, Y.; Tang, J.; Kang, G.; Miao, H. Circumferential SH Wave Piezoelectric Transducer System for Monitoring Corrosion-Like Defect in Large-Diameter Pipes. Sensors 2020, 20, 460. https://doi.org/10.3390/s20020460

[115] Kinsler, L. E., Frey, A. R., Coppens, A. B., & Sanders, J. V. (2000). Fundamentals of acoustics. John wiley & sons.

[116] J. Bao and V. Giurgiutiu, "Lamb Wave Generation and Detection with Piezoelectric Wafer Active Sensors" Dissertation Paper for Degree of Doctor of Philosophy in the Department of Mechanical Engineering College of Engineering and Information Technology University of South Carolina 20," in An Initial Investigation of the Large Strain and Fatigue Loading Behavior of Piezoelectric Wafer Active Sensors", SPIE's 12th International Symposium on Smart Structures and Materials and 10th International Symposium on NDE for Health Monitoring and Diagn, 2003, pp. 7–10

[117] Dorafshan, S., Thomas, R. J., & Maguire, M. (2018). Fatigue crack detection using unmanned aerial systems in fracture critical inspection of steel bridges. Journal of Bridge Engineering, 23(10), Article 04018078.

[118] Dorafshan, S., Maguire, M., Hoffer, N. V., & Coopmans, C. (2017). Fatigue Crack Detection Using Unmanned Aerial Systems in Under-Bridge Inspection. Boise, ID, USA: Idaho Transportation Department.

[119] Roberge, P. R. (2007). Corrosion inspection and monitoring. John Wiley & Sons.

[120] Ivošević, Š., Kovač, N., Momčilović, N., & Vukelić, G. (2022). Evaluation of the Corrosion Depth of Double Bottom Longitudinal Girder on Aging Bulk Carriers. Journal of marine science and engineering, 10(10), 1425.

[121] Zhang, H., Du, Y., Tang, J., Kang, G., & Miao, H. (2020). Circumferential SH wave piezoelectric transducer system for monitoring corrosion-like defect in large-diameter pipes. *Sensors*, *20*(2), 460.

[122] Kubrusly, A. C., von der Weid, J. P., & Dixon, S. (2019). Experimental and numerical investigation of the interaction of the first four SH guided wave modes with symmetric and non-symmetric discontinuities in plates. NDT & E International, 108, 102175.

[123] Pau, A., & Achillopoulou, D. V. (2017). Interaction of shear and Rayleigh–Lamb waves with notches and voids in plate waveguides. Materials, 10(7), 841.

[124] Demma, A., Cawley, P., & Lowe, M. (2003). Scattering of the fundamental shear horizontal mode from steps and notches in plates. The Journal of the Acoustical Society of America, 113(4), 1880-1891.

[125] Viktorov, I. A. (1967). Rayleigh and Lamb Waves—Physical Theory and Application. New York, NY: Plenum Press.

[126] Achenbach, J. D. (1973). Wave Propagation in Elastic Solids: North-Holland Series in Applied Mathematics and Mechanics. Amsterdam, The Netherlands: Elsevier.

[127] Graff, K. F. (1975). Wave Motion in Elastic Solids. London, UK: Dover Publications.

[128] Rose, J. L. (1999). Ultrasonic Waves in Solid Media. Cambridge, UK: Cambridge University Press.

[129] Dieulesaint, E., & Royer, D. (1996). Ondes Élastiques Dans Les Solides—Tome 1: Propagation Libre et Guidée. Paris, France: Masson.